University of Basel
Department of Physics

Transport in graphene

Master's Thesis

Nikolas A. Minder

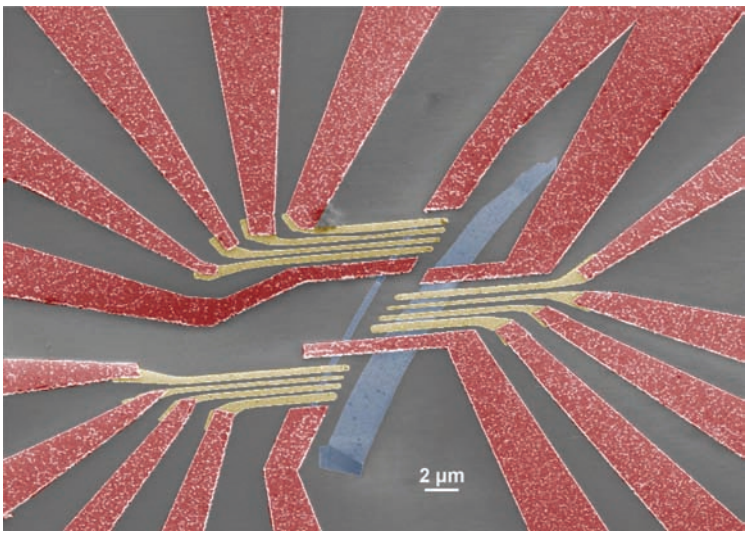

Supervisors:

Dr. J. Trbovic
Prof. Dr. C. Schönenberger

· Basel, November 21, 2008 ·

Our long-term goal is to study spin and coherence effects in hybrid graphene devices consisting of ferromagnetic and superconducting electrodes on single layer graphene (F/G/S structures), as shown in the scanning electron micrograph on the title page. Graphene is inherently different from semiconductors or metals, e.g. due to its linear dispersion relation. Therefore, well-known effects as Andreev reflection (AR) in normal metal/superconducting junctions are expected to behave differently in graphene. As an outlook, one can think of investigating non local AR or the quantum spin Hall effect in such a device. In order to study hybrid devices, it is important to first understand the individual components.

During the course of this master thesis, we investigated the electronic properties of F/G/F and S/G/S structures at cryogenic temperatures. Single layer graphene flakes were contacted by electron beam lithography followed by metal evaporation. We observed half-integer conductance plateaus in the quantized Hall regime, magnetoresistive switching, as well as Andreev reflections.

Contents

1. Introduction

Allotropes of carbon – one of the most abundant element in living organisms – have been known for thousands of years in form of diamond and graphite. With the discovery of spherical fullerenes in 1985 [1] and of cylindrical nanotubes in 1991 [2], the family of all-carbon modifications increased and received much attention from theoretical and experimental scientists. The discovery of single-atom thick carbon sheets in 2004 [3] revived the excitement for this versatile element. The two-dimensional crystal known as graphene, exhibits auspicious material properties, owing to its high crystal quality and unique electronic spectrum [4]. In the late 1930s, Peierls [5] and Landau [6] introduced the notion that 2D materials were thermodynamically unstable. Yet, out-of-plane corrugations of the 2D crystal as shown in figure 1.1 suppress thermal vibrations and prevent graphene from melting [7].

Graphene's peculiar electronic structure – arising from the honeycomb-like arrangement of carbon atoms – results in novel physical properties and renders the 2D crystal an interesting material to study not only quantum mechanical, but also relativistic-like effects.

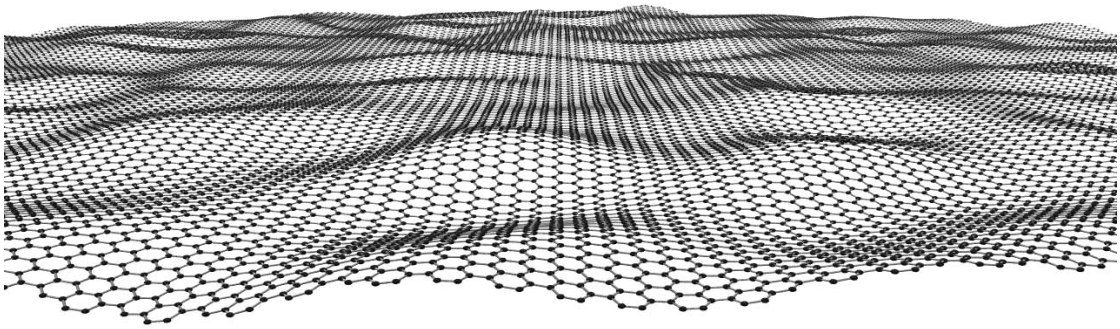

FIGURE 1.1.: Illustration of a single-layer graphene sheet with out-of-plane corrugations. The thermodynamic stability of the 2D crystal is believed to be accounted for mainly by such ripples [7]. (Image source: J. Meyer [7])

Graphene is considered a possible alternative to silicon (Si)-based semiconductor devices, such as Si MOSFETs, as it exhibits high mobilities, is stable at small dimensions,

shows a strong electric field effect for confined geometries [8] or bilayer graphene [9] and – most importantly – is potentially cheap to produce. One major obstacle for industrial implementation is large area production of single or bilayer graphene. This could be solved by the chemical vapor deposition (CVD) technique: epitaxial growth of few-layer graphene has been shown [10] and could help pave the way towards electronic applications.

Graphene is also a promising candidate for spintronic devices: due to the low spin-orbit and hyperfine interactions of the 2D crystal, graphene devices exhibit spin relaxation lengths up to several micrometers [11].

The following chapter gives a short theoretical introduction to graphene's electronic properties as well as the physical effects relevant for this project. Chapter 3 describes the experimental work, the results of our measurements are presented in chapter 4, while chapter 5 focuses on conclusions from the experiments and gives an outlook to future experimental work.

2. Background

This chapter first outlines the physical properties of graphene, particularly its electronic structure, followed by a short introduction to the main aspects of the quantum Hall effect in graphene, electronic spin transport and Andreev reflection.

2.1. Graphene

Graphene is a single layer of hexagonally arranged carbon atoms, owing its thermodynamic stability largely due to out-of-plane corrugations (see figure 1.1) which suppress thermal vibrations and prevent it from melting [7]. The true monolayer nature of graphene can be verified using Raman spectroscopy [14], quantum Hall effect measurements [15, 16] or to some extent atomic force microscopy (AFM) [12, 13].

Graphene belongs to the class of fullerene allotropes or "graphitic materials", composed solely of sp^2-bonded carbon atoms. *Graphite* is the three-dimensional analogue made up of stacked graphene sheets. Figure 2.1 schematically shows carbon allotropes of different dimensions.

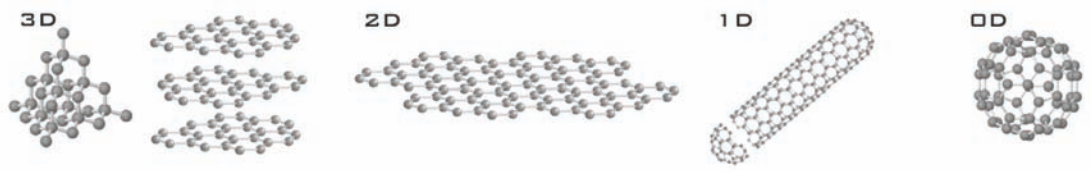

FIGURE 2.1.: **Graphitic materials.** 3D: sp^3-bonded diamond (left) and graphite, which consists of stacked layers of 2D graphene sheets. 1D: nanotubes can be imagined as rolled up graphene, whereas 0D Buckminsterfullerenes (buckyballs) represent wrapped graphene sheets. (Image source: M. Katsnelson [17])

The sp^2-bonds in graphene arise from hybridization of carbon's valence electrons, such that the $2s$ and the $2p$-orbitals of three neighboring carbon atoms mix and form sp^2 orbitals. Consequently, the atoms in graphene are arranged in a trigonal planar geometry giving it an overall hexagonal ("honeycomb") lattice. In bulk graphite, the length a_0 of a C–C bond is 1.418 Å and the inter-layer spacing $d_0 = 3.347$ Å. The

remaining valence electrons form π-bonds perpendicular to the sp^2-plane. Electrons in the π-bonds are delocalized and form a conjugated system in which they can move freely. These π electrons are primarily responsible for graphene's band structure.

2.1.1. Electronic band structure

The band structure of graphene was derived in 1947 using the tight binding model [18]. In this section, only the result is discussed, while the interested reader is referred for example to refs. [19] or [20].

Using a Bloch wave ansatz:

$$\psi_{\vec{k}} = \sum_{\vec{R}} e^{i\vec{k}\vec{R}} \phi(\vec{x} - \vec{R}) \tag{2.1}$$

where ϕ are the one-electron atomic wavefunctions (p_z orbitals), the following energy dispersion relation is obtained:

$$E(k_x, k_y) = \pm\gamma_1 \sqrt{1 + 4cos\left(\frac{3a_0}{2}k_y\right) cos\left(\frac{\sqrt{3}a_0}{2}k_x\right) + 4cos^2\left(\frac{\sqrt{3}a_0}{2}k_x\right)} \tag{2.2}$$

The two solutions correspond to the bonding ($-$) and anti-bonding ($+$) orbitals. The two energy bands touch each other at six points at the edges of the (hexagonal) Brillouin zone. These points, referred to as K and K$'$ points (resulting from the two-atomic basis of graphene's hexagonal lattice), lie at the Fermi energy E_F (see figure 2.2). Graphene is considered a zero-gap semiconductor and as in conventional semiconductors, the charge carrier density n can be tuned by electrical gating, thereby moving the fermi level E_F.

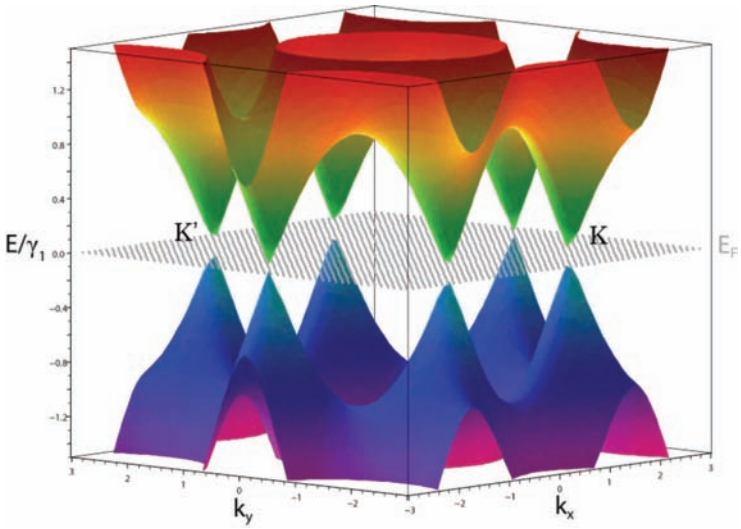

FIGURE 2.2.: Energy dispersion relation ("band structure") of graphene. The valence and conduction bands touch at the K and K$'$ points in **k**-space.

2.1.2. Dirac fermions

A peculiarity of graphene is that its charge carriers do not show the typical parabolic dispersion relation $E(\mathbf{k}) = \hbar^2\mathbf{k}^2 \cdot (2m^*)^{-1}$ characteristic of free electrons or electrons in metals and semiconductors. Instead, due to the honeycomb lattice, graphene shows a linear dispersion relation

$$E(k) = \pm\hbar|\mathbf{k}|\nu_{\mathrm{F}} \tag{2.3}$$

in the vicinity of the K and K′-points, as shown in figure 2.2 ($\nu_{\mathrm{F}} \approx 10^6$ m·s^{-1} is the Fermi velocity). Such a linear energy relation is also described by the Dirac equation, where

$$\hat{H} = \hbar\nu_{\mathrm{F}} \begin{pmatrix} 0 & k_x - ik_y \\ k_x + ik_y & 0 \end{pmatrix} = \hbar\nu_{\mathrm{F}}\hat{\sigma} \cdot \mathbf{k} \tag{2.4}$$

is the Dirac hamiltonian ($\hat{\sigma}$ are the 2D Pauli matrices and $\mathbf{k}$ is the quasiparticle momentum) [4]. Because of the formal analogy to the Dirac equation, the electrons in graphene are often referred to as Dirac fermions and the corners of the Brillouin zone are called Dirac points. If we calculate the (isotropic) effective mass

$$m^* = \hbar^2 \left(\frac{\partial^2 E}{\partial k^2} \right)^{-1} \tag{2.5}$$

using the energy from eq. (2.3), we find that m^* vanishes. The same result is obtained by comparing the energy of a Dirac particle (eq. 2.3) to the relativistic energy $E = \sqrt{p^2c^2 + m_0^2c^4}$. If one substitutes the particle's momentum $p = \hbar\mathbf{k}$ and the effective speed of light $c = \nu_{\mathrm{F}}$, the rest mass m_0 vanishes. The zero effective mass for a range of wave vectors implies that for low energies ($E < 1$ eV [4]), electrons and holes do not interact with the crystal lattice [21].

2.2. Quantum Hall Effect (QHE)

Classically, an electrical conductor carrying a current I in a perpendicular magnetic field $B_\perp$ will show a potential difference $U_{xy} = U_H$ across the opposite sides of the conductor. The hall resistance $R_H = U_H/I = -B_\perp/(net)$ is the ratio of the potential drop divided by the current, where n is the charge carrier density, e is the electron charge, and t is the thickness of the conductor. The Hall effect is a consequence of the Lorentz force acting on the charge carriers: the transverse magnetic field deflects the carriers, causing them to accumulate at one side of the conductor.

In two dimensional electron gases (2DEGs) at low temperatures and high magnetic fields, it was found [23] that the Hall conductivity $\sigma_H = \rho_H^{-1}$ takes on discrete values of

$$\sigma_H = N \cdot \frac{\nu e^2}{h}, \quad N = 0, 1, 2, \ldots \tag{2.6}$$

where where h is the Planck constant, e is the electron charge and ν is the degeneracy of the 2DEG. This is due to the fact that in a perpendicular magnetic field, the electrons in the 2DEG are forced to move in quantized cyclotron orbits with discrete energy levels. These energies, known as Landau levels (LLs), are given by

$$E_N = (N + 1/2)\hbar\omega_c, \tag{2.7}$$

where $\omega_c = eB/m^*$ is the cyclotron frequency. The Hall conductivity σ_H is remains constant when the Fermi energy E_F is between two LLs and increases by a discrete value, when E_F passes the passes the next higher LL (by electrically gating the 2DEG).

2.2.1. QHE in graphene

The QHE in single layer graphene (SLG) differs from that in conventional 2DEGs in the sense that the Hall conductivity plateaus are shifted [4] and form at

$$\sigma_H = (N + \frac{1}{2})\frac{4e^2}{h}, \quad N = 0, 1, 2, \ldots \tag{2.8}$$

This so-called half-integer QHE of SLG was first measured by Novoselov *et al.* [15] (see figure 2.3) and Zhang *et al.* [16]. The reason for this shift of $2e^2/h$ is that in graphene, the LL energies are given by

$$E_N = \pm\nu_F\sqrt{2e\hbar BN}. \tag{2.9}$$

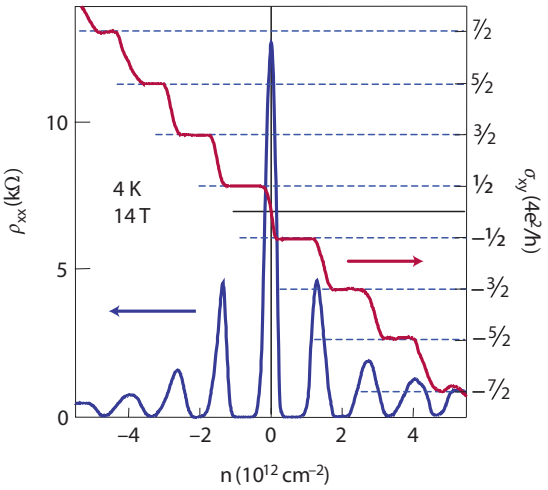

FIGURE 2.3.: QHE measurements at 4 K/14 T of a single layer graphene device by Novoselov *et al.* [15]. The Hall conductivity $\sigma_{xy} = \rho_H^{-1}$ as a function of the carrier concentration n forms plateaus at half-integer values of $4e^2/h$ (red curve), while the longitudinal resistivity ρ_{xx} vanishes at these values of n (blue curve). Adopted from Geim *et al.* [4].

The zero-energy LL for $N = 0$ is a consequence of the pseudospin structure of graphene, giving rise to a phase shift of π when the electrons perform a circular rotation (Berry phase) [24].

2.2.2. Two-terminal quantum Hall conductance

Quantum Hall measurements offer a reliable tool to verify single layer graphene. However, fabrication of two additional electrodes – needed to measure the Hall conductivity – next to an actual device is often unpractical or even impossible since many structures require closely spaced contacts and graphene flakes are often too small for additional structures. Fortunately the anomalous quantum Hall effect of graphene is also seen in two-terminal devices in which the current path coincides with the voltage probe circuit [25, 26]. In such a setup, the measured conductance $G = dI/dV$ is function of the Hall conductivity σ_{xy} as well as the longitudinal conductivity $\sigma_{xx} = \rho_{xx}^{-1}$.

Recent two-terminal measurements of the QHE in graphene devices with different geometry show a strong dependence of G on the aspect ratio L/W of the devices [25, 27] (L is the length and W the width of the graphene conductor). The influence of geometry on the two-terminal quantized Hall conductance of monolayer and bilayer graphene devices was studied theoretically by Abanin *et al.* [28]. Starting from the transport equation $\mathbf{j}=\hat{\sigma}\mathbf{E}$, they came up with a model which predicts the two-terminal conductance of graphene in the quantum Hall regime by using only the aspect ratio L/W and a LL broadening parameter λ as inputs. Starting from the known analytic result for the conductance of a square [29]

$$G_{L=W} = \sqrt{\sigma_{xx}^2 + \sigma_{xy}^2}, \tag{2.10}$$

they used the semicircle model for the microscopic transport coefficients σ_{xy} and σ_{xx} developed by Dykhne *et al.* [30] to analyze arbitrarily shaped[1] graphene monolayer and bilayer samples in the quantized Hall regime. The main steps derived by Abanin *et al.* are listed below. The quantum Hall plateaus in single layer graphene are centered at charge carrier densities

$$\nu_n = 4(n + 1/2)\frac{|B|}{\Phi_0}, \quad n = 0, \pm1, \pm2, \ldots, \tag{2.11}$$

with the single LL electron density $|B|/\Phi_0$ ($\Phi_0 = h/2e$ is the flux quantum).

The semicircle model [30] relates the contributions of each LL to the longitudinal and Hall conductivities $\delta_n\sigma_{xx}(\nu)$ and $\delta_n\sigma_{xy}(\nu)$ as

$$\delta_n\sigma_{xx}^2 + (\delta_n\sigma_{xy} - \sigma_{xy,n}^{(0)})(\delta_n\sigma_{xy} - \sigma_{xy,n'}^{(0)}) = 0, \tag{2.12}$$

[1] Conductors of arbitrary shape can be reduced to conduction problems of rectangular geometry using conformational mapping [31].

where $\sigma^{(0)}_{xy,n'}$ and $\sigma^{(0)}_{xy,n'}$ are the Hall conductivities of adjacent plateaus[2]. The broadening of the LLs are modeled by a Gaussian distribution of the longitudinal conductivity,

$$\delta_n \sigma_{xx}(\nu) = 2e^{-\lambda[\nu - 1/2(\nu_n + \nu_{n'})]^2} \tag{2.13}$$

where λ is the LL width parameter. The total longitudinal and Hall conductivities

$$\sigma_{xx}(\nu) = \sum_n \delta_n \sigma_{xx}(\nu), \quad \sigma_{xy}(\nu) = \sum_n \delta_n \sigma_{xy}(\nu) \tag{2.14}$$

are illustrated in figure 2.4.

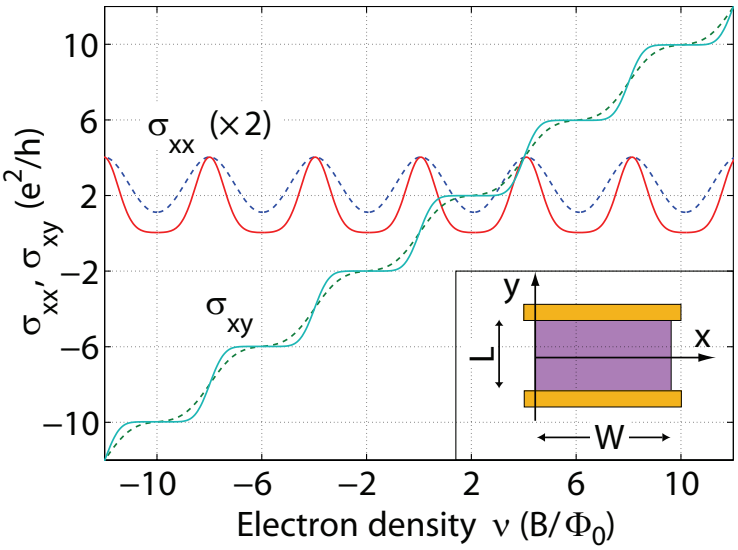

FIGURE 2.4.: **Calculated longitudinal and Hall conductivities σ_{xx} and σ_{xy}** versus electron density ν for monolayer graphene as described in the main text. Solid and dashed lines correspond to weak and strong LL broadening (LL width parameters $\lambda = 1.7$ and $\lambda = 0.5$). The plateaus of σ_{xy} are at $(N + 1/2)4e^2/h$, where $N = 0, 1, 2, \ldots$. The two-terminal sample geometry is illustrated in the inset. Adopted from Abanin *et al.* [28].

The components E_y and E_x of the electric field at a point $z = x + iy$ were found [32] to be the real and imaginary parts of the analytic function

$$E_y + iE_x = -e^{f(z)}, \quad f(z) = i\theta - \sum_{n>0(odd)} \frac{4\theta}{n\pi} \frac{sinh(n\pi iz/W)}{cosh(n\pi L/2W)} \tag{2.15}$$

where $\theta = tan^{-1}(\sigma_{yx}/\sigma_{xx})$ is the Hall angle. Integration of the current distribution – obtained by combining the relation

$$j_x + ij_y = (\sigma_{xx} + i\sigma_{yx})(E_x + iE_y) \tag{2.16}$$

with eq. (2.15) – along a cross section through the sample, yields the total current I. For

[2] n and n'$= n+1$ follow the sequence $\ldots, -2, -1, 0, 1, 2, \ldots$ for monolayer graphene.

the geometry shown in the inset of figure 2.4, it is easiest to integrate along the x-axis ($y = 0$). Using eq. (2.16),

$$I = \int_0^W j_y(x,0)dx = \int_0^W \sigma_{xx}[E_y(x,0) + tan(\theta)E_x(x,0)]dx. \tag{2.17}$$

The voltage drop V between the source and drain contacts ($y = \pm L/2$ in the schematics of figure 2.4) is conveniently integrated along $x = W/2$, thus

$$V = \int_{-L/2}^{L/2} E_y(W/2,y)dy. \tag{2.18}$$

To calculate the two-terminal conductance $G = I/V$, the integrals (2.17) and (2.18) have to be solved numerically. Figure 2.5 shows calculated conductance versus electron density plots of SLG for different aspect ratios L/W as well as LL width parameters λ [28].

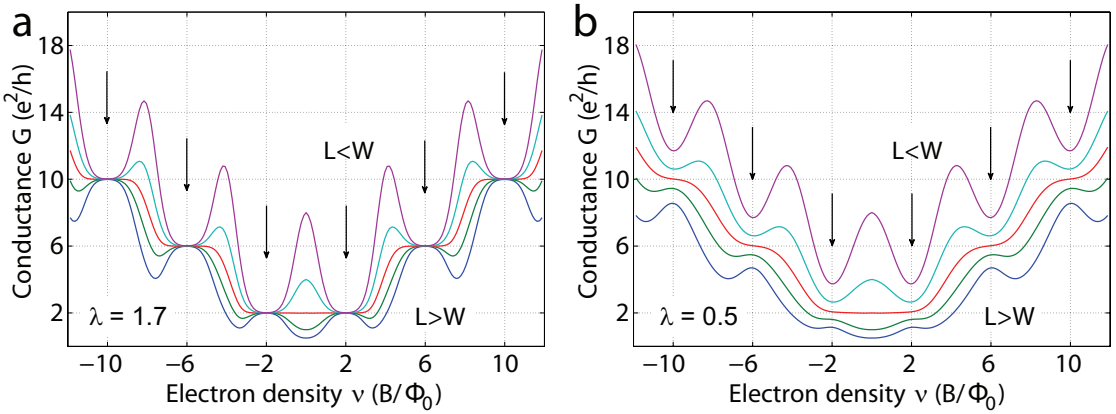

FIGURE 2.5.: **Calculated two-terminal conductance of SLG in the quantum Hall regime.** The sample aspect ratio $L/W = 0.25, 0.5, 1, 2, 4$ (top to bottom) strongly influences the two-terminal conductance G through SLG. **a**) For weak ($\lambda = 1.7$) LL broadening, the conductance plateaus match the values expected from eq. (2.8). Arrows indicate the carrier densities ν given by eq. (2.11). Between the plateaus, G is enhanced for $L/W < 1$ and decreased for $L/W > 1$ due to the different influence of σ_H and σ_{xx}. **b**) For increased LL broadening ($\lambda = 0.5$), the positions of the conductance plateaus (minima for $L/W < 1$ and maxima for $L/W > 1$) are not affected, but there is an increase (decrease) in G for decreasing (increasing) L/W. Image adopted from Abanin *et al.* [28].

The model derived by Abanin *et al.* was found to be in good general agreement with two-terminal quantum Hall conductance measurements [27]. In some cases, the actual aspect ratios L/W differed significantly from the calculated values. A possible explanation for these discrepancies might be, that the contacts either locally dope the graphene or do not inject the current homogenously. This would lead to smaller widths W and therefore to different aspect ratios. Close to the charge neutrality point, density fluctuations due to electron and hole puddles could also influence the conductivity. In summary, it can be said that the model describes the significant features of two-terminal QHE measurements and entitles these as a reliable method to distinguish between monolayer, bilayer and multi-layer graphene.

2.3. Spin transport in mesoscopic systems

Spintronic devices make use of magnetoresistance (MR) effects, such as Hall effects [22], anisotropic magnetoresistance (AMR) [33], tunneling magnetoresistance (TMR) [34] or giant magnetoresistance (GMR) [35, 36]. The latter effects are observed in thin film structures containing two ferromagnetic materials separated by a normal metal (GMR) or insulating (TMR) spacer. These devices show higher current-perpendicular-to-plane (CPP) resistances if the ferromagnetic layers are aligned antiparallel than for parallel alignment. Such structures, called *spin-valves*, are used industrially as non-volatile magnetic sensors such as hard drive read heads. The working principle is illustrated in figure 2.6. The resistance through the two ferromagnetic layers (F1 and F2), which are sepa-

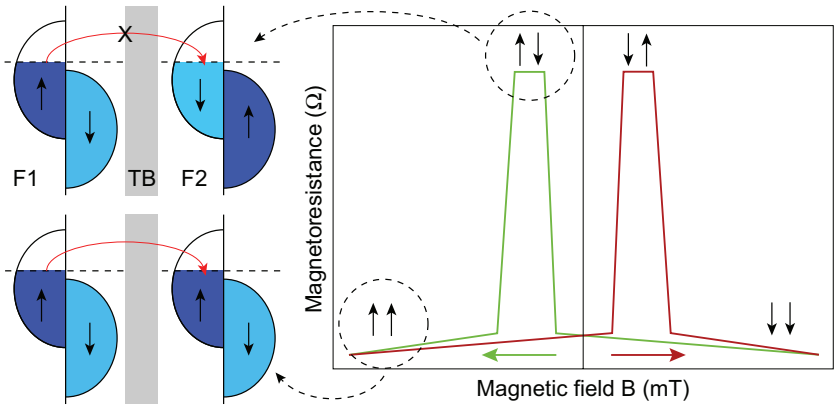

FIGURE 2.6.: **Illustration for the magnetoresistance of a spin valve.** A device consists of two ferromagnetic layers, F1 and F2, which are separated by a thin insulating layer acting as a tunneling barrier (TB). The magnetoresistance through the device depends on the relative magnetic orientation of F1 and F2, which is changed from parallel (↑↑) to antiparallel (↑↓ or ↓↑) by applying a magnetic field B. For antiparallel alignment of the ferromagnets, electrons can only tunnel from F1 into free states of F2 when they flip their spin, whereas for parallel alignment, electrons can tunnel without spin-flip. Therefore, the resistance is lower for parallel than for antiparallel alignment.

rated by a tunneling barrier (TB), depends on the relative magnetic orientation of F1 and F2. The relative orientation can be changed from parallel (↑↑) to antiparallel (↑↓ or ↓↑) by applying a magnetic field B. The tunneling magnetoresistance is lower for parallel than for antiparallel alignment, since electrons tunneling from F1 into F2 have to flip their spin in the case of antiparallel alignment.

Important aspects for designing spintronic devices, i.e. devices based on manipulation of the spin degree of freedom [37] include spin injection and accumulation, spin coherence times and lengths, as well as spin manipulation. A prerequisite for spintronic applications

is the ability to create spin-polarized currents with a preferred, or majority, spin species.

The spin polarization $\alpha = \frac{N_\uparrow - N_\downarrow}{N_\uparrow + N_\downarrow}$ determines the ratio of spin-polarized charge carriers $N_{\uparrow,\downarrow}$ to the total number of carriers ($0 \leq \alpha \leq 1$, $N_{\uparrow(\downarrow)}$ is the number of carriers with magnetic moment parallel (antiparallel) to the direction of magnetization). Natural candidates for creating spin-polarized currents are ferromagnetic materials (metals or semiconductors), since $N_\uparrow \neq N_\downarrow$ at the fermi energy.

Spin transport in a device consisting of a non-magnetic conductor contacted by ferromagnetic leads (F/N/F spin valve) can be explained by spin accumulation and spin relaxation. When injecting spins from a ferromagnetic metal F into a non-ferromagnetic conductor N (such as graphene), there is spin accumulation at the F/N interface: since the majority and minority spin conductivities are unequal in the ferromagnets ($\sigma_\uparrow \neq \sigma_\downarrow$), a charge current $I = I_\uparrow + I_\downarrow$ produces a spin current $I_s = I_\uparrow - I_\downarrow$. However, the conductivities of spin-up and spin-down particles in N are equal, causing spins to accumulate at the interface [38]. This interfacial spin imbalance creates a potential gradient $\Delta\mu_s = \mu_\uparrow - \mu_\downarrow$ in addition to the electrochemical potential gradient $\Delta\mu_{ch} = \mu^{Source} - \mu^{Drain} = e \cdot V$ between two contacts. The potential difference $\Delta\mu_s$ is called *induced magnetization* or *spin accumulation*. Unlike charge, spin is not a conserved quantity. Therefore, spin accumulation will decay on a timescale given by the spin relaxation time τ_{sf} due to spin-flip processes. On average, injected spins will diffuse towards decreasing electrochemical potentials. Yet, due to spin relaxation, the chemical potentials $\mu_{\uparrow,\downarrow}$ decay exponentially over a certain length, characterized by the spin relaxation length $\lambda_{sf} = \sqrt{D\tau_{sf}}$, where D is the diffusion constant [38].

2.4. BCS Superconductivity

Superconductivity is an electronic phenomenon occurring in certain materials such that below a critical temperature T_c, electrons of opposite spin pair up into so-called Cooper pairs and form a Bose-Einstein condensate. Since the Cooper pairs have zero total spin, they behave like bosons and don't interact with the lattice, resulting in zero electrical resistance. The BCS theory, describing superconductivity on a microscopic level, was derived in 1957 by Bardeen, Cooper and Schrieffer. In particular, it is able to explain the energy gap between the ground state and the quasi-particle excitations, as observed in normal metal/superconducting (N/S) junctions. For energies $E < \pm\Delta$, there are no single-particle states available in the superconductor (S), so electrons from the normal metal (N) cannot tunnel in. This implies that a source-drain bias voltage $V_{SD} \geq \Delta/e$ has to be applied for a current to flow. The BCS theory states that the zero-temperature energy gap is $\Delta(T = 0) = 1.76 k_B T_c$.

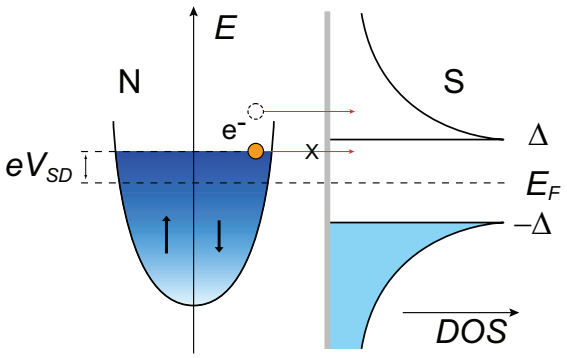

FIGURE 2.7.: Illustration of the density of states (DOS) for a normal conductor/superconductor (N/S) interface. In S, there is a superconducting energy gap, which prevents electrons with energies $E < \pm\Delta$ from tunneling through the N/S interface. By applying a bias voltage $V_{SD} \geq \Delta/e$, electrons can tunnel from N into the empty states in S.

2.4.1. Andreev reflection (AR)

Andreev reflection (AR) is a charge-transfer process occurring at N/S interfaces, by which an electron excitation (filled state at energy ε above the Fermi energy E_F) is converted into a hole excitation (empty state at energy $E_F - \varepsilon$). As mentioned above, the existence of the energy gap at $E_F \pm \Delta$ in the density of states of a superconductor classically prevents transfer of single quasi particle states with an energy $|\varepsilon| < \Delta$. However, including second order processes, an incoming electron can be transferred into S if

a Cooper pair is formed together with a second electron[3]. In terms of single excitations, this process is equivalent to the creation of an Andreev reflected hole [39].

Andreev reflection depends strongly on the N/S interface. This is illustrated in figure 2.8 for three different interface transparencies, characterized by a parameter Z. For clear

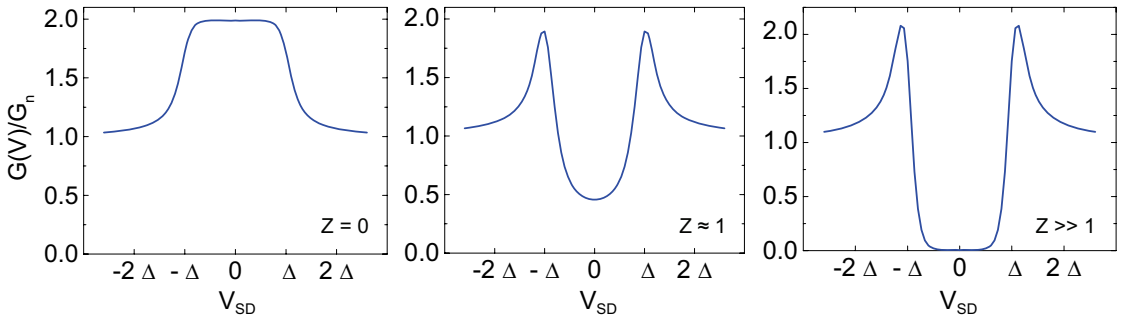

FIGURE 2.8.: **Illustration of Andreev reflection (AR) at N/S interfaces**. Normalized differential conductance $G(V)/G_n$ as a function of the bias voltage V_{SD} for clear metallic contacts (Z=0), semi-opaque junctions (Z≈1) and tunnel barriers (Z≫1). For Z=0, a doubling of the conductance is expected, while for increasing opacity of the interface, the conductivity is lowered in the gap. Adopted from J. Trbovic.

interfaces ($Z = 0$), AR leads to doubling of the conductance in the region of the energy gap (sub-gap conductance), while for increasing Z, the conductance is decreased inside the gap. Tunnel barriers are described by $Z \gg 1$.

The peculiarity of AR in graphene is that at N/S interfaces, holes are retro-reflected, while AR is specular for graphene/S junctions. Detailed discussion of AR in graphene is beyond the scope of this thesis and can be found, for example, in a recent review by Beenakker et al. [40].

[3]In this process, the Cooper pair absorbs the charge of $2e$ created when an electron of charge $-e$ is reflected into a hole of charge e.

3. Experimental techniques

Graphene samples were prepared by peeling graphite flakes from highly oriented pyrolytic graphite (HOPG) crystals with adhesive tape and pressing them onto a Si/SiO_2 wafer. Graphene monolayers were located using optical microscopy, evaporation masks for electrically contacting the flakes were written with electron beam lithography (EBL) and the contacts were evaporated in ultra-high vacuum by electron beam or thermal evaporation. The fabrication steps are briefly described in the following sections, while detailed instructions are given in appendix A.

3.1. Substrate preparation

In order to locate and contact graphene flakes, an orientation grid is needed on the substrate. Usually this is done by writing a matrix of cross-like markers using electron beam lithography (EBL) and then evaporating Ti/Au [41]. Because the grid area needed is large ($\sim$1$\times$1 cm^2), writing markers with EBL will is very time consuming. Therefore, a new mask for UV lithography was designed to decrease the production time of the orientation grid.

As substrates, highly doped Si wafers[1] with a 300 $\pm$ 5 nm thick layer of thermally oxidized SiO_2 were used. After sonication in acetone and isopropanol (IPA), the substrates were blow-dried with nitrogen gas (N_2) and spin-coated with photoresist, followed by soft-baking on the hot plate.

The markers are 18 μm by 26 μm in size and are spaced 200 μm from each other. The matrix is made up such that the two numbers to the left of the cross represent the row and the right numbers represent the column. So for instance, $\frac{2|3}{8|1}$ is the matrix element in row 28 and column 31 (starting with $\frac{1|1}{1|1}$ in the top left corner). The UV mask consists of 100 by 100 markers, resulting in a total applicable area of 2$\times$2 cm^2. Using e-beam evaporation, a 10 nm thick adhesion layer of Ti was deposited at room temperature in high vacuum, followed by a 40 nm thick layer of Au. Lift-off was done at room temperature in acetone, leaving well-defined markers.

[1] Paul Scherrer Institut, Villigen, Switzerland

3.2. Flake deposition and localization

Before deposition of graphene flakes, the substrate was cleaned by reactive ion-etching (RIE) in Ar/O_2 atmosphere. Single-layer graphene flakes were produced by exfoliation of highly-oriented pyrolytic graphite (HOPG)[2], i.e. continuous peeling of graphite flakes with Nitto tape. When the flakes seemed sufficiently thinned out (after roughly 5 to 10 peeling steps), they were brought onto a freshly cleaned substrate by firmly pressing the tape onto the wafer. After removing the tape, the samples were rinsed in acetone and IPA and blow-dried N_2.

Single-layer graphene flakes were localized under an optical microscope. Single-layer graphene laying on a 300 nm thick SiO_2 layer can be detected using conventional (white-light) optical microscopy due to interference effects [42].

Pictures of the flakes with four surrounding markers were taken with a digital camera (figure 3.1a). After converting the photographs to monochromatic bitmap files (figure 3.1b) the bitmap to cif converter of the *CleWin* package was used to automatically create mask layouts (figure 3.1c), which were then edited in *CleWin*.

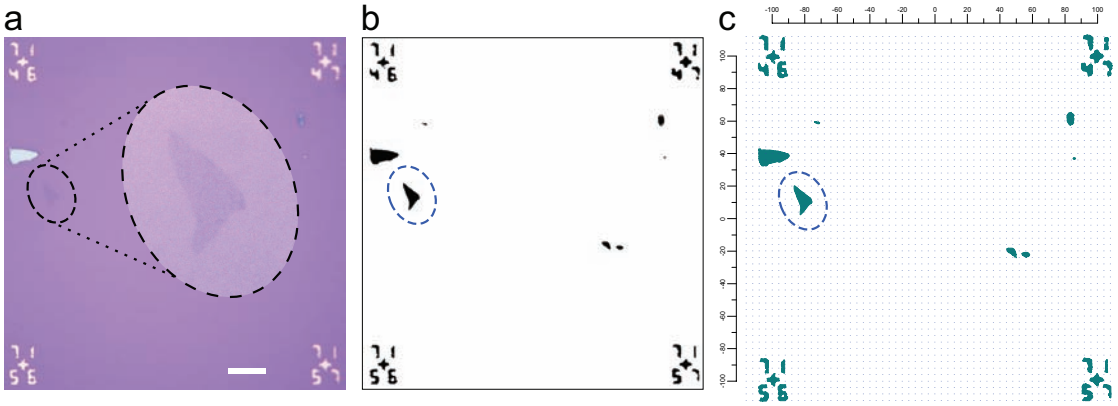

FIGURE 3.1.: **Creating a mask layout. a**) Image of a graphene flake (enlargement in dashed frame) surrounded by four alignment markers. Scale bar is 25 μm. The image is then saved as a black and white bitmap file (**b**) and converted to a mask layout (**c**) using the bitmap to cif converter of the *CleWin* package.

3.3. Contact fabrication

During deposition of graphene and localization of flakes under the microscope, the sample is subject to various sources of contamination. Under the atomic force microscope

[2] University of Manchester; origin: North Korea

(AFM), the graphene flakes appear dirty and their actual height is masked by contaminations on the surface. We found that 1 h of vacuum annealing at 400° C significantly decreased the roughness and the apparent height of the graphene flakes.

After thermal annealing, a thin film ($\sim$ 300 nm) of *Polymethyl methacrylate* (PMMA)[3] was brought onto the samples by spin-coating, followed by baking in an oven.

After loading the sample into the scanning electron microscope (SEM), the beam current was measured with a faraday cup setup. The beam was focused on the PMMA surface using (granular) silver paint and the sample stage of the SEM was centered and aligned underneath the electron beam using the markers for orientation. The structures was typically written in two steps, using a 120 μm aperture together with the M30/2000 μm^2 lens for large structures such as bonding pads for wire bonds and a 10 μm aperture with the M240/250 μm^2 lens for small structures like the electrodes contacting the graphene flakes. After exposure[4], development was done in MIBK[5]/IPA (3:1 v/v).

Metal evaporation was done either by e-beam or thermal evaporation. While the thermal evaporator reaches higher evaporation rates of a few angstroms per second, the e-beam system allows for a better vacuum below $5 \cdot 10^{-10}$ mbar as well as cooling of the sample holder down to liquid nitrogen temperature. After evaporating a 5 nm Ti adhesion layer, either Al, Pd or PdNi and Co were evaporated, depending on the sample and process step.

3.4. Measurements

The sample holder loaded into the cryostat is a 1×1 cm^2 carbon sample holder with 20 Au contacts. Connecting the sample holder contacts with the evaporated metal contacts on the sample was done with an ultrasonic wedge bonder[6] using a 25 μm Al wire. The bonding parameters[7] were determined such that bonding would not punch through the SiO_2 layer (causing the contacts to short with the Si back-gate) but still hold firmly [43].

Electrical measurements of the samples were performed in the "Cryolab" using SR830 DSP lock-in amplifiers[8] at a low frequencies ($<$ 100 Hz), as well as a Yokagawa 7651

[3] 950K positive e-beam resist, Allresist GmbH, Strausberg, Germany
[4] Acceleration voltage: 20 kV, stage height: 11 mm, area dose: 250 μAs$\cdot$ cm^{-2}, area step: 8/32 nm.
[5] *Methyl isobutyl ketone*
[6] 4523AD, Kulicke and Soffa, Fort Washington, VA
[7] **1**st **bond**: Search: 1.95, Power: 1.56, Time: 3.9, Force: 1.3, Step: 3.5, Kink: 0.0, Reverse: 0.0, Yspeed: 1.0, Loop: 2.7
2nd **bond**: Search: 1.13, Power: 1.68, Time: 5.9, Force: 1.4, Tail: 1.5, Tear: 3.0
[8] Stanford Research, Sunnyvale, CA

DC voltage source[9]. The two-point resistances of all samples were first measured in air and at room temperature to check for functioning. Low-temperature measurements were performed in a *HelioxVL* ^{3}He sorption cryostat (Oxford Instruments) as well as a ^{4}He cryostat (Cryogenics). Both cryostats have built-in superconducting coils to apply (vertical) dc magnetic fields. To reduce noise, capacitor-input filters (π-filters) were utilized and unused wires were capped.

After cryogenic measurements, the samples were examined by SEM using an acceleration voltage of 5 kV and a working distance of 5 mm.

[9] Yokogawa Electric Corporation, Tokyo, Japan

4. Results

In this section, we present the the low-temperature measurements performed in the *Cryolab* of our fabricated devices. Before inserting a sample into the cryostat, the 2-terminal resistances of the contacts were measured at room temperature and in air and electrical gating of the flakes was checked in vacuum.

Our research platform is single layer graphene (SLG) which shows unique half-integer QHE (see section 2.2). The measurements of three samples with interesting results are shown in the following sections.

4.1. Evidence for single layer graphene flakes

The following graphene sample with ferromagnetic Co contacts (NM063) showed no AMR and only weak MR signals when applying an in-plane magnetic field parallel to the contact electrodes. A strong electric field effect was observed as shown in figure 4.1. The pronounced (Dirac) peak is a strong indication of a single-layer graphene

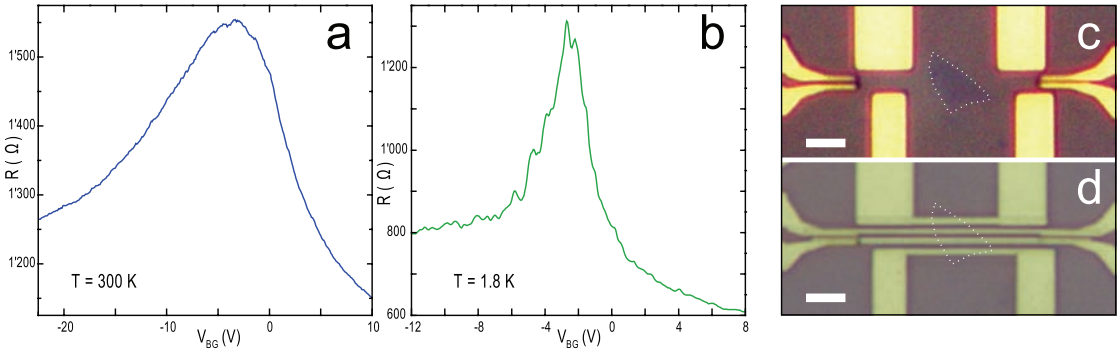

FIGURE 4.1.: Two-terminal resistance R versus back-gate voltage V_{BG} of sample NM063 at 1.8 K (**a**) and at room temperature (**b**). The Dirac point is around -2.5 V and the curve is slightly asymmetric in the electron and hole region. As the sample shows a strong back-gate dependence already at room temperature, we expected the flake to be single-layer graphene. Figures **c** and **d** are optical microscope images after evaporation of the normal metal leads (**c**) and the Co electrodes (**d**). The graphene flake is indicated by dotted lines, the scale bars represent 2.5 μm.

(SLG) flake, since the electric field effect in multi-layer graphene is much weaker due to

screening [25]. To verify the single-layer nature of the flake, we applied a perpendicular magnetic field of 8 T and measured the back-gate dependence of the conductance.

4.1.1. Two-terminal quantum Hall effect (QHE) measurements

As mentioned in section 2.2.2, the half-integer quantum Hall effect of SLG can also be observed in two-terminal devices.

In a current-biased setup, we first measured the two-terminal resistance of the device as a function of the magnetic field $B_\perp$ and the back-gate voltage V_{BG}. At high magnetic fields ($B_\perp \geq 4$ T), we started observing resistance plateaus which became more pronounced with increasing field (see figure 4.2a).

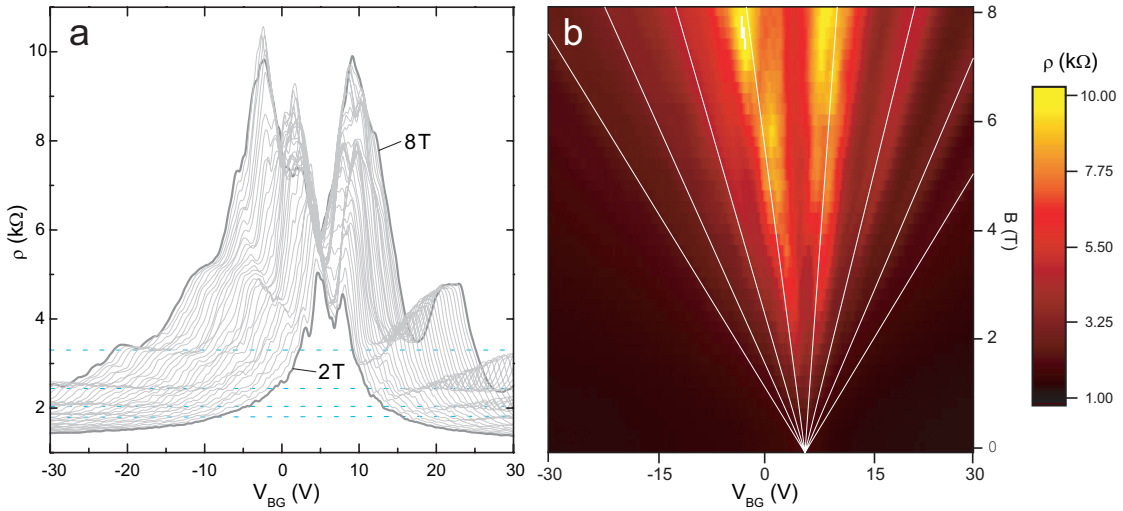

FIGURE 4.2.: Two-terminal resistivity ρ measured as a function of back-gate voltage V_{BG} and magnetic field $B_\perp$ at $T = 230$ mK. **a**) $\rho\,(V_{BG})$ plotted for increasing $B_\perp$ from 2 T to 8 T (ΔB = 200 mT). Dashed lines indicate plateaus in ρ. **b**) Colorscale plot of the resistivity ρ versus back-gate voltage and magnetic field. White lines indicate evolving plateaus.

To check for half-integer quantum Hall plateaus, we measured the conductance G at $B_\perp = 8$ T in a voltage biased setup ($V_{ex} = 20\ \mu$V). We observed pronounced conductance plateaus, yet the values of G neither matched the half-integer plateaus of SLG given by eq. (2.8) nor those for bilayer graphene ($\sigma_N = N \cdot 4e^2/h,\ N = 1, 2, \ldots$). We assume that the total resistance R_{tot} measured is comprised of the contributions of longitudinal and Hall resistivities from graphene, $\rho_G = \rho_{xx} + \rho_H$, plus a contact resistance R_C. To determine the contribution of ρ_G to the total resistance R_{tot}, the contact resistance R_C at a given field $B_\perp$ has to be subtracted from R_{tot}. At the Hall plateaus, there is no contribution from the longitudinal resistivity, so the ρ_G depends only on the Hall

resistivity, given by

$$\rho_G = \sigma_H^{-1} = \left(\frac{e^2}{h} \cdot \nu \right), \tag{4.1}$$

where the filling factor

$$\nu = 4\left(N + \frac{1}{2}\right), \quad N = 0, 1, 2, \ldots \tag{4.2}$$

The total resistance thus can be expressed as

$$R_{tot} = \rho_G + R_C = \frac{h}{e^2} \cdot \frac{1}{\nu} + R_C. \tag{4.3}$$

For $1/\nu \to 0$, the left part of equation 4.3 vanishes and thus the contact resistance can be determined from $\lim_{n\to\infty} R_{tot} = R_C$. The above discussed procedure is shown in figure 4.3 for a conductance measurement at 8 T and 240 mK. The local peaks of the total resistance $R_{tot} = G^{-1}$ as a function of the charge carrier density ($n_{2D} = V_{BG} \cdot 6 \cdot 10^{10}$ cm^{-2}V^{-1} as taken from previous studies [12]) show a linear dependence on the inverse of the filling factor, ν^{-1}.

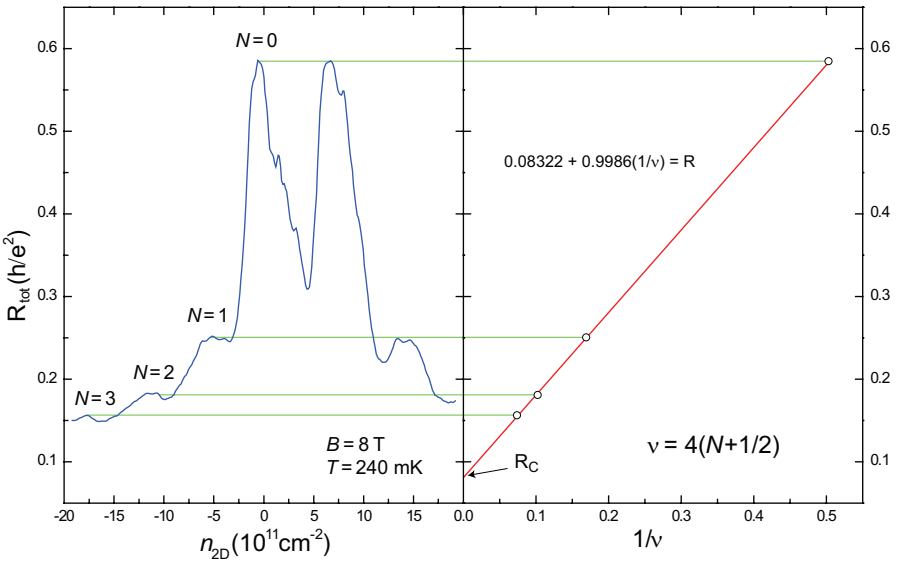

FIGURE 4.3.: **Determining the contact resistance R_C by extrapolation ($1/\nu \to 0$).** The total resistance R_C for the first four LLs are plotted as a function of $1/\nu$, where $\nu = 4(N + \frac{1}{2})$ is the filling factor. The linear fit yielded an intercept at $R_C = 0.08322\ h/e^2 \approx 2'148\ \Omega$. (An induced charge carrier density n_{2D} of $6{\cdot}10^{10} cm^{-2}$ per 1 V of V_{BG} was assumed [12].)

After subtraction of $R_C \approx 2'148\ \Omega$, the conductance plateaus were identified at half-integer multiples of $4e^2/h$ as shown in figure 4.4.

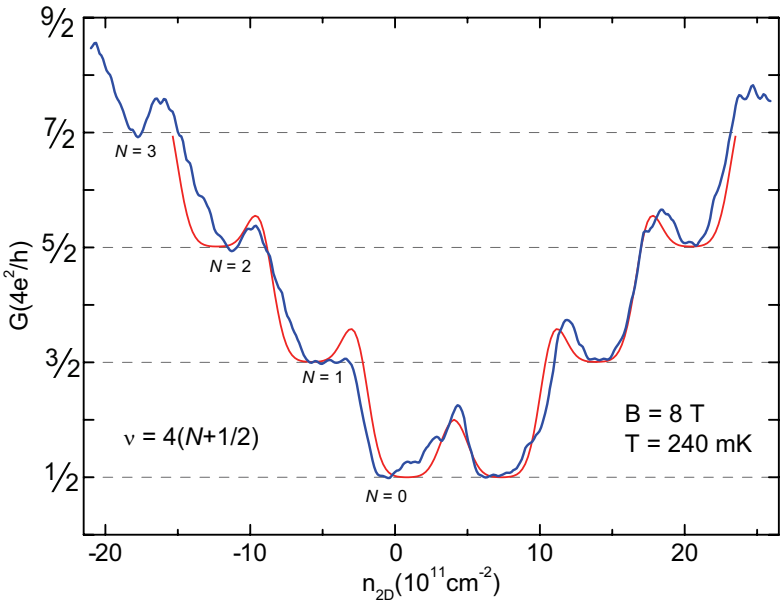

FIGURE 4.4.: Two-terminal conductance G versus carrier density n after subtraction of the calculated contact resistance R_C as described in the main text. The measurements taken at $T = 240$ mK and a magnetic field $B = 8$ T (blue curve) show the first four LL plateaus at half-integer values of $4e^2/h$, characteristic of single layer graphene. The red curve is an overlay of the calculated conductance from eqs. (2.17) and (2.18) for an aspect ratio L/W of 0.5 and a LL broadening parameter $\lambda = 1.7$ ([28]). From optical microscopy, we estimate an actual aspect ratio of the device of approximately 0.3.

The calculated two-terminal conductance for weak LL broadening and an aspect ratio $L/W = 0.5$ (red curve), which was taken from [28] and overlayed, is in good qualitative agreement with the experimental data and the inter-plateau conductance peaks are well reflected. The actual aspect ratio of the device is approximately 0.3, therefore the conductance peaks are expected to be slightly higher than for $L/W = 0.5$ (see figure 2.5a).

There is an asymmetry between the electron and hole regions, such that the conductance in the hole region is generally slightly lower and the peak between the $N = 0$ and $N = 1$ plateaus is missing. The plateaus become less pronounced with increasing N, as observed by others [25, 27]. The calculated two-terminal conductance for strong LL broadening ($\lambda = 0.5$, see figure 2.5b) fit the higher conductance plateaus better but poorly matched the area around the $N = 0$ plateaus, which is better described by weak LL broadening. This discrepancy is possibly due to varying LL broadening for different charge carrier densities n, which is not considered in the model [28].

4.1.2. Additional plateaus

One of the features of two-terminal quantum Hall effect measurements is the central peak between the two lowest conductance plateaus. We observed additional sub-plateaus between the two N=0 LLs (see figure 4.4), which cannot be explained by the model by Abanin *et al.* We used the previously described method (linear dependency of $R = G^{-1}$ on $\frac{1}{\nu}$) to calculate the values of $\nu = 0.9986 \cdot (\rho - 0.08332)^{-1}$ and $N = \nu/4 - 1/2$ for these sub-plateaus found that the values of N correspond to approximately 1/6 and 2/6.

R_{tot} (h/e^2)	ν	N
0.4569097	2.672	$0.168 \approx 1/6$
0.3827068	3.334	$0.334 \approx 2/6$

TABLE 4.1.: Calculated values of N for the values ρ of the sub-plateaus between the two N=0 LLs.

At the moment, we do not have any explanation for these sub-plateaus. They might be contact-specific (in our case Co) or result from inhomogeneities of the SLG flake, but further investigations are necessary to understand this phenomenon.

4.2. Graphene with ferromagnetic contacts

The following sample (NM052) consisted of a few-layer graphene flake contacted by four ferromagnetic $Pd_{0.25}Ni_{0.75}$/Co/Pd electrodes (25/40/10 nm) on Ti/Au leads (10/40 nm). Two of the ferro-electrodes (B and D in figure 4.5b) were contacted at both sides to measure the magnetization switching fields of the electrodes.

After cooling down the sample in the ^{3}He cryostat, we measured the two-terminal resistance as a function of back-gate voltage V_{BG}. A broad Dirac peak was observed as shown in figure 4.5, presumably due to a multi-layer graphene flake.

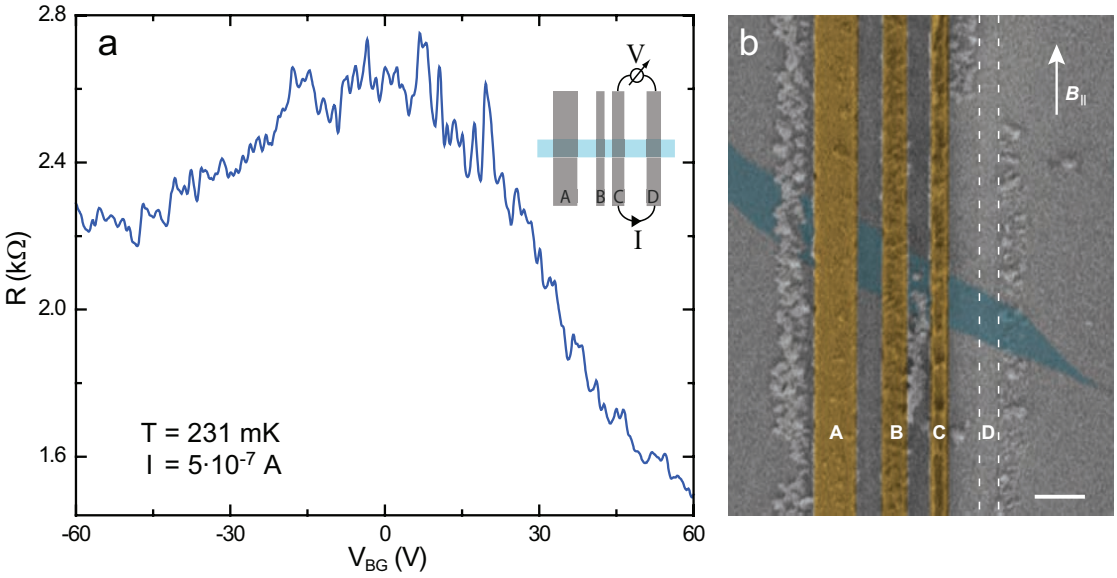

FIGURE 4.5.: **Graphene flake contacted by ferromagnetic electrodes.** **a**) Two-terminal back-gate sweep of sample NM052 showing a weak resistance dependence on the applied electric field as expected for multi-layer graphene. **b**) Scanning electron micrograph of the device with a graphene flake (colored in blue) contacted by PdNi/Co/Pd electrodes (colored in yellow). A parallel magnetic field $B_{\parallel}$ was applied in the measurements. Electrode D, indicated by the dashed lines, was destroyed during the measurements. The widths of the electrodes are 425 nm (A), 275 nm (B), 165 nm (C), and 300 nm (D); scale bar represents 500 nm. The residue on the side of the electrodes appeared after lift-off; its origin could not be determined.

4.2.1. Anisotropic magnetoresistance (AMR) measurements

The switching fields B_{sw} were determined by applying an external dc magnetic field parallel to their long axis of the electrodes ($B_{\parallel}$) while measuring the two-terminal resistance R over the electrodes. Due to anisotropic magnetoresistance (AMR)[1], R depends on the angle Θ between the magnetization of the electrode $\boldsymbol{M}$ and the current density

[1] $R = R_{\parallel} - sin^2\Theta \cdot (R_{\parallel} - R_{\perp})$

$\boldsymbol{j}$. The resistance is maximal when $\boldsymbol{M}$ is parallel (or antiparallel) to $\boldsymbol{j}$. By inverting $B_{\parallel}$, a torque acts on $\boldsymbol{M}$ which rotates it in the direction of the external field. When $\boldsymbol{M}$ is perpendicular to $\boldsymbol{j}$, $R = R_{\perp}$ becomes minimal.

After sweeping the magnetic field multiple times between ± 500 mT in order to magnetize the magnetic domains of the electrodes parallel to the long axis, we measured $R\left(B_{\parallel}\right)$ in a current-biased setup (I_{ac} = 500 nA). For the 275 nm wide electrode, we found a switching field B_{sw}^{B} of approximately 24 ± 2 mT, while the 300 nm wide electrode switched at $B_{sw}^{D} \approx 20 \pm 2$ mT (see figure 4.6). The magnitude of the AMR signals

$$\Delta R = \frac{R_{\parallel} - R_{\perp}}{R_{\parallel}} \tag{4.4}$$

is approximately 0.25 %.

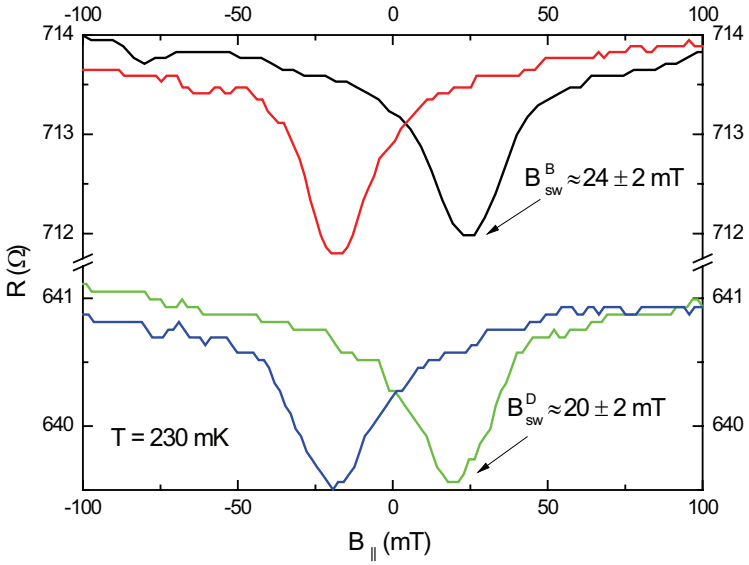

FIGURE 4.6.: **Anisotropic magnetoresistance (AMR) measurements.** $R\left(B_{\parallel}\right)$ signals of two ferromagnetic PdNi/Co/Pd electrodes showing a negative AMR signal as expected in a parallel magnetic field. Electrode B with a width of 275 nm switches at $B_{sw}^{B} \approx 24$ ±2 mT (black and red curves), while electrode D of width 300 nm switches at $B_{sw}^{D} \approx 20$ ±2 mT (green and blue curves).

4.2.2. Magnetoresistance through graphene

While sweeping $B_{\parallel}$, we measured the resistance through the graphene flake in different configurations. Due to spin polarization of the ferromagnetic contacts, a spin-polarized current will be injected into graphene. The total resistance R_{tot} through the device is given by the resistance of the leads, the contact resistances, the resistance from graphene

and a magnetoresistive component which is dependent on the magnetization $\boldsymbol{M}$ of the ferro-electrodes, as well as spin relaxation in graphene. In order to exclude the lead and contact resistances of the device, we measured the (classical) four-terminal resistance by passing a current through the outer two electrodes and measuring the voltage drop over the inner two electrodes using a high input impedance.

Figure 4.7, shows classical four-point resistance measurements as a function $B_{\|}$ at 1.7 K. We observed four switching events $B^i_{sw} \approx 7$, 20, 25, 32 mT. From AMR measurements, the switching fields of 20 mT and 25 mT can be attributed to switching of contacts D and B. Since the coercive field of a magnet is inversely proportional to its width w, $B_{sw} \sim w^{-1}$, the two resistance jumps at 7 mT and 32 mT can be assigned to magnetization switching of contacts A and C.

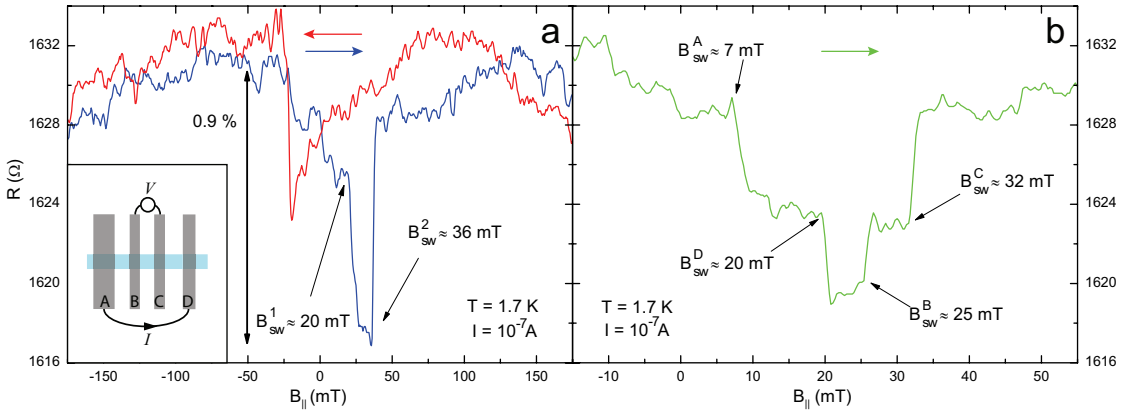

FIGURE 4.7.: **Classical four-point measurements at 1.7 K. a**) Trace (blue curve) and retrace (red curve) of the classical four-terminal resistance $R = V/I$ (see inset) as a function of the magnetic field $B_{\|}$. A negative magnetoresistance (MR) of approximately 0.9 % is observed and two switching fields $B^{1,2}_{sw}$ can be determined. The sample temperature was 1.7 K, the current I was 100 nA and the scan rate was 60 mT/min. **b**) At lower scan rates (15 mT/min), four switching events $B^i_{sw} = 7$, 20, 25, 32 mT are observed. From the AMR measurements (see figure 4.6a), the switching fields of 20 mT and 25 mT can be attributed to switching of contacts D and B. Since B_{sw} of a ferromagnet is inversely proportional to its width, the events at 7 mT and 32 mT can be assigned to switching of contacts A and C.

To determine the spin signal, we measured the non-local voltage drop V_{nl} over two electrodes spatially separated from the current circuit. Figure 4.8 shows MR measurements in the local two-point (**a**) and non-local (**b**) configurations. We observed an unexpectedly high [11] background resistance in the non-local measurements, which – during later SEM imaging – could be traced to touching of the adjacent electrodes B and C (see inset in 4.8b)

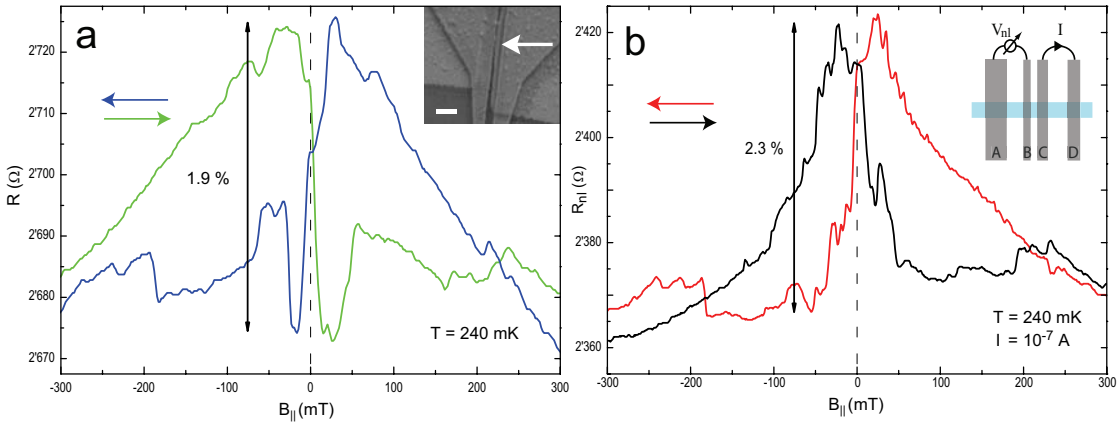

FIGURE 4.8.: **Comparison of non-local and local measurements at 240 mK. b**) While passing a current $I = 10^{-7}$ A through contacts C and D, the resistance $R_{nl} = V_{nl}/I$ was measured in a non-local setup over contacts A and B (see inset in **b**). The black and red curves are the trace and retrace from negative to positive $B_{\|}$ and vice versa, showing a MR of ∼2.3 %. The large background resistance of approximately 2.3 kΩ is not expected for non-local MR signals [11] and is comparable in shape to the two-terminal $R(B_{\|})$ measurements over contacts B and C shown in **a**. The arrow in the inset of **a** indicates where electrodes B and C are touching. Scale bar is 500 nm.

Since two of the electrodes were in contact, the measured resistance cannot be attributed to the non-local spin signal.

4.3. Graphene with superconducting contacts

This section shows the measurements of sample NM041 (figure 4.9) on which a graphene nanoribbon was contacted by superconducting Ti/Al/Ti electrodes (5/40/20 nm). At room temperature, we measured two-point resistances between 7 kΩ and 17 kΩ. After cooling down the sample in the ^{3}He cryostat to 4.2 K, the two-point resistances increased (e.g., from 7.8 kΩ to 11.6 kΩ for the electrodes with a center-to-center distance $d = 915$ nm as shown in figure 4.9). One contact was not working anymore, presumably due to loosening of a wire bond during cool-down. From the SEM image, we estimated the width w of the graphene ribbon between 150 nm and 200 nm.

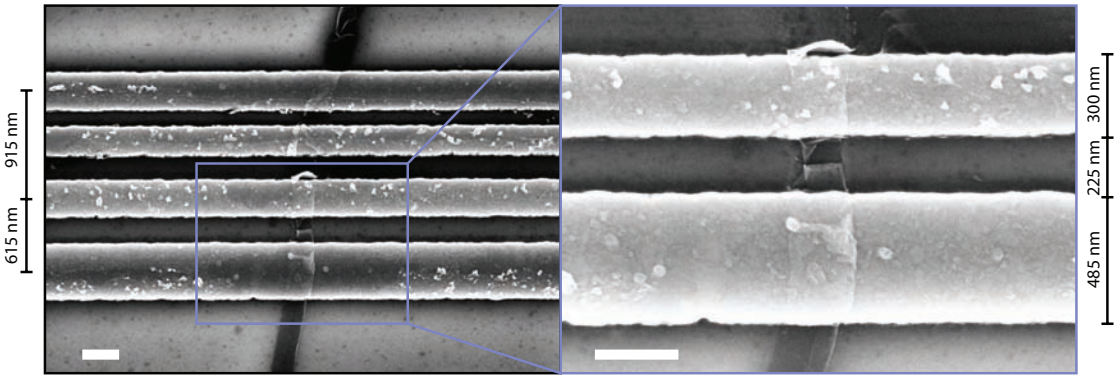

FIGURE 4.9.: Scanning electron micrograph of sample NM041 with four Ti/Al/Ti electrodes across a multi-layer graphene nanoribbon (left) and magnification of the framed area. In the micrograph on the right, folding of the graphene ribbon can be seen. The center-to-center distances of the two electron pairs measured in this sample are 615 nm and 915 nm, while the corresponding edge-to-edge spacings d are 225 nm and 580 nm. Both scale bars correspond to 300 nm.

4.3.1. Conductance measurements of a narrow S/G/S device

Transport properties of the device was mapped by measuring the two-terminal differential conductance $G = dI/dV$ as a function of bias voltage V_{SD} and back-gate voltage V_{BG} (see figure 4.10). These measurements were first done above the superconducting transition temperature ($T_c \approx 1.11$ K from measurements in a similar device, see appendix B) of the Ti/Al/Ti leads. While superimposing an ac excitation voltage $V_{ex} = 25$ μV on V_{SD}, the (pre-amplified) ac current through the device was measured with the lock-in amplifier.

We measured the conductance between the two pairs of leads first with $d_1 = 225$ nm and second with $d_2 = 580$ nm. The center-to-center spacings between the two working pairs of superconducting contacts are 615 nm and 915 nm and the edge-to-edge distances d are 225 nm and 580 nm.

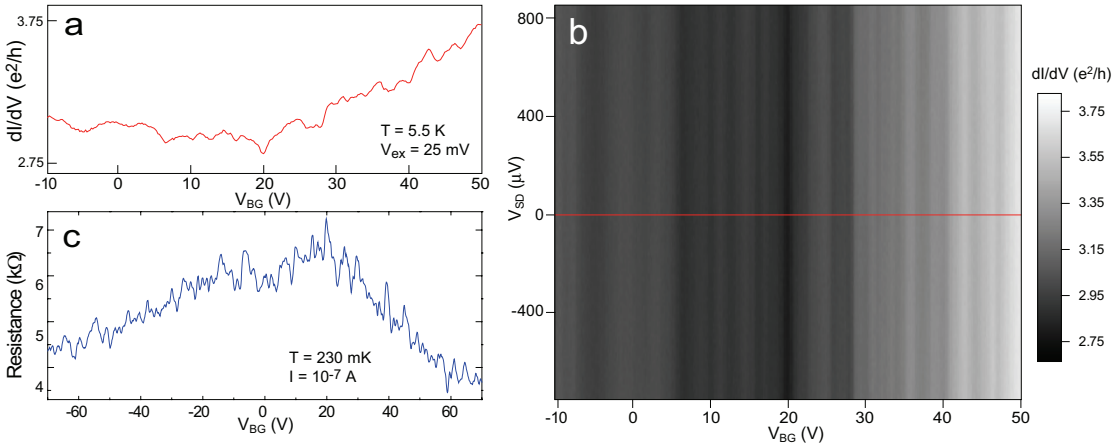

FIGURE 4.10.: **a**) Two-terminal conductance $G = dI/dV(V_{SD} = 0\,V)$ for the narrow spaced contacts ($d = 225\,\text{nm}$) as a function of back-gate voltage V_{BG}. The device shows a broad Dirac peak, characteristic of multi-layer graphene. The strong fluctuations presumably arise from universal conductance fluctuations (UCF), as the narrow graphene ribbon has width w of approximately 150 - 200 nm. The UCF is more pronounced in the three-terminal resistance measurements (**c**), where a current $I = 10^{-7}$ A was passed between the outer two contacts and the resistance $R = V/I$ was measured over the closer contact pair ($d = 225\,\text{nm}$). **b**) In the grayscale plot recorded at $T = 5.5$ K, above the superconducting transition temperature of the Ti/Al/Ti contacts, we observed no source-drain bias dependence over the entire back-gate region between -10 V and +50 V.

The conductance $G(V_{BG})$ of the shorter contact pair at $T \approx 5.5$ K (above the critical temperature of the Ti/Al/Ti contacts) is shown in figure 4.10a. We noticed pronounced universal conductance fluctuations (UCF) in the gate dependance of G, which is even more prominent in three-terminal current-biased resistance measurements (4.10c). In the grayscale conductance plot 4.10b, we note that G is constant as the bias voltage V_{SD} is swept for fixed back-gate voltages. This drastically changes, as the temperature is lowered to 230 mK, below T_c. An energy gap opens in the superconductor and graphene is subject to the proximity effect [44].

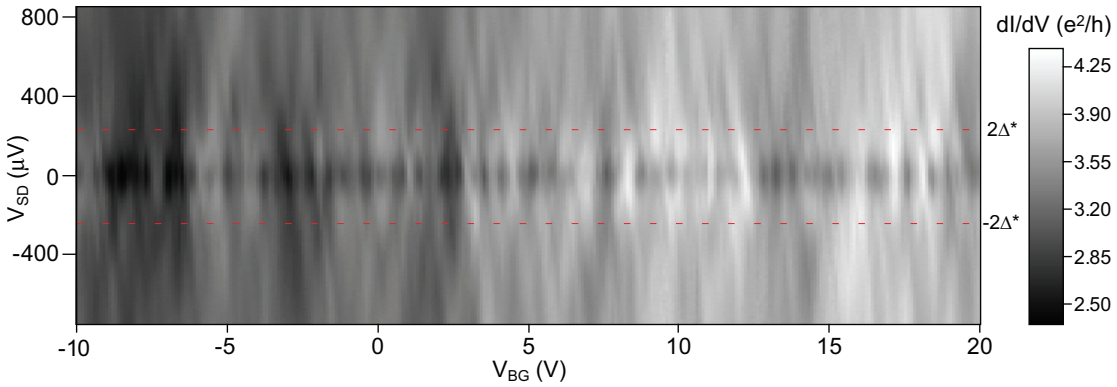

FIGURE 4.11.: Grayscale plot of the conduct dI/dV as a function of the back-gate voltage V_{BG} and the bias voltage V_{SD} at $T = 230$ mK. Besides the zero-bias conductance dip (superconducting gap) over a wide range of gate voltages, there are some values of V_{BG} which show zero-bias conductance peaks. The dashed red lines indicate the superconducting gap $2\Delta^*$.

We observed oscillations of the sub-gap conductance, modulated by the back-gate voltage as shown in figure 4.11. There are some back-gate regions, for which the zero-bias conductance is increased and we attribute this behavior to Andreev reflection. Figure 4.12 shows typical $dI/dV(V_{SD})$ traces for different values of V_{BG} (-9.6, -7.7, -1.2, 1.1, 2.9, 17.1 V) which have conductance gaps (V_{BG}= -7.7 V, -1.2 V and 1.1 V) and peaks (V_{BG}= -9.6 V, 2.9 V and 17.1 V,) around V_{SD}=0 V.

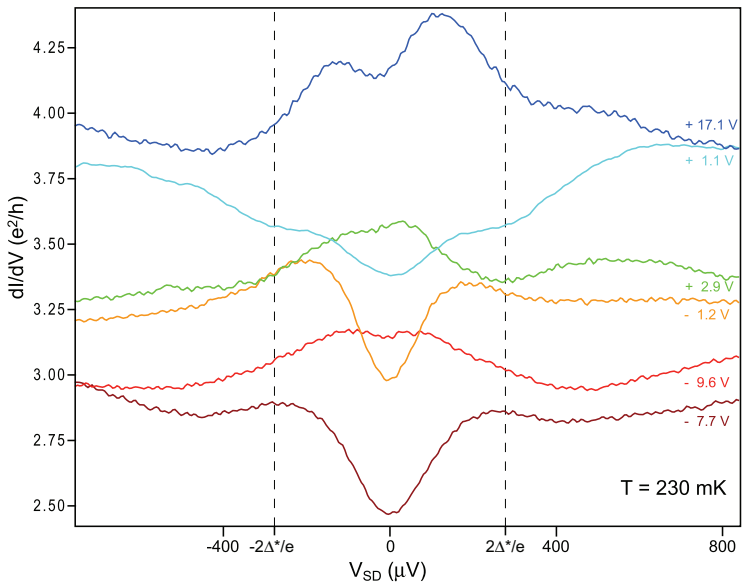

FIGURE 4.12.: Typical bias voltage V_{SD} traces at various back-gate voltages V_{BG}. For gate voltages of -7.7 V, -1.2 V and 1.1 V, the superconducting gap can be seen, while for V_{BG}= -9.6 V, 2.9 V and 17.1 V, the conductance is increased due to Andreev reflections. From the traces, we estimate a superconducting gap of $2\Delta^*/e \approx 300$ μV for this device.

The estimated superconducting gap $2\Delta^* \approx e \cdot 300$ μV is in agreement with the theoretical zero-temperature superconducting gap $\Delta_0^{BCS} = 1.76 k_B T_c \approx 168$ μeV.

In the superconducting state, the conductance was also measured for the wider contact pair ($d = 580$ nm). Due to the limited superconducting coherence length ξ, which we estimate to approximately 200 nm, the transport properties are expected to change with increasing spacing d of the superconducting contacts. Compared to the narrow contact pair, the pair with increased spacing shows lower conductance and a less distinct superconducting gap (figure 4.13). Presumably, the barrier between the contacts and the graphene ribbon is responsible for the broad conductance dip. Because the spacing $d = 580$ nm is larger than our estimate of the superconducting coherence length, we expect a weaker proximity effect in graphene, leading to a decreased conductance compared to the narrow pair of contacts (see caption of figure 4.13).

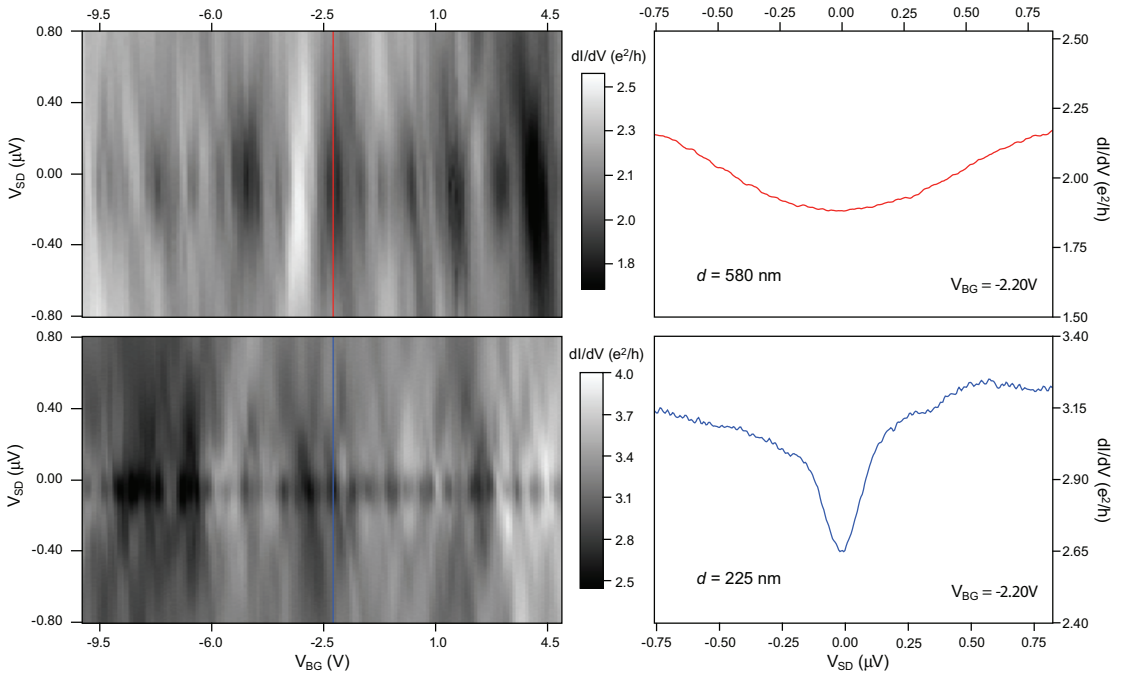

FIGURE 4.13.: **Distance dependence on the superconducting gap.** Conductance (dI/dV) grayscale plots for different contact spacing d (left images) and characteristic V_{SD} traces at a gate voltage of - 2.20 V (right images). For the closer contacts with an edge-to-edge distance $d = 225\,\text{nm}$ (lower trace) the conductance is higher and there is a more defined gap ($0.60\ e^2/h$) than for the wider contacts with $d = 580\,\text{nm}$ spacing ($0.29\ e^2/h$).

4.3.2. Magnetic field dependence

The effect of a parallel magnetic field was investigated in two different regions showing increased and decreased zero-bias conductance by applying an external magnetic field B_{ext}. The zero-bias conductance peak monotonously decreases with increasing field, while in zero-bias conductance dip initially increases for low B_{ext} and decreases at higher fields as shown in figure 4.14.

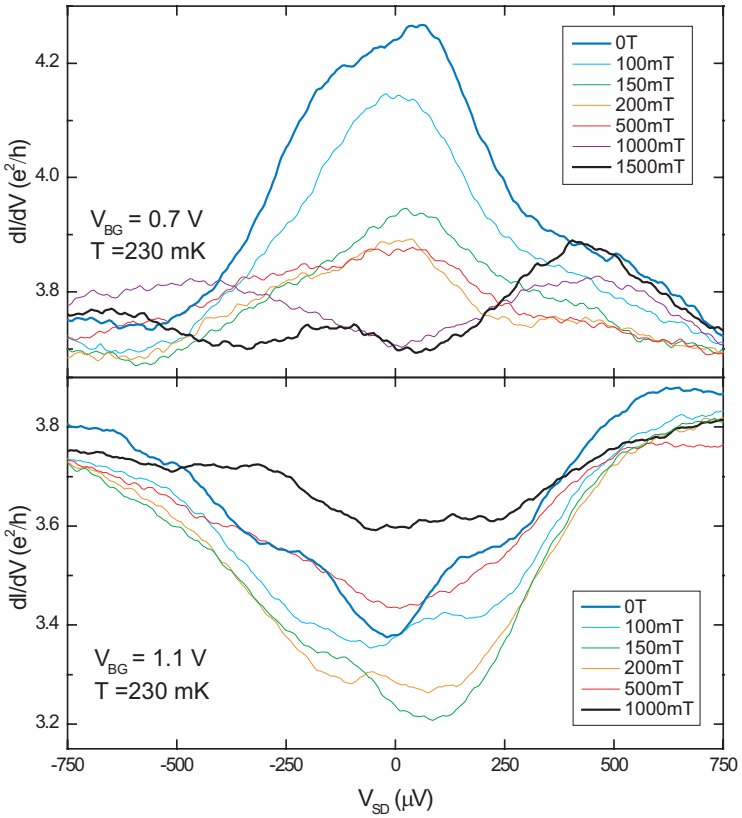

FIGURE 4.14.: In-plane magnetic field (B_{ext}) dependence of bias voltage (V_{SD}) sweeps. The upper (lower) graph shows the evolution for a conductance peak (dip) from 0 T to 1.5 T (1 T). Both measurements were performed at T = 230 mK and fixed back-gate voltages V_{BG} of 0.7 V (upper graph) and 1.1 V (lower graph). Note that the traces at 1 T approximately coincide for the two gate voltage regions.

4.3.3. Additional conductance traces for the narrow contact pair

Figure 4.15 shows additional $dI/dV(V_{SD})$ traces of the 225 nm spaced contacts for various values of V_{BG} showing gap (upper graph) and peak features (lower graph).

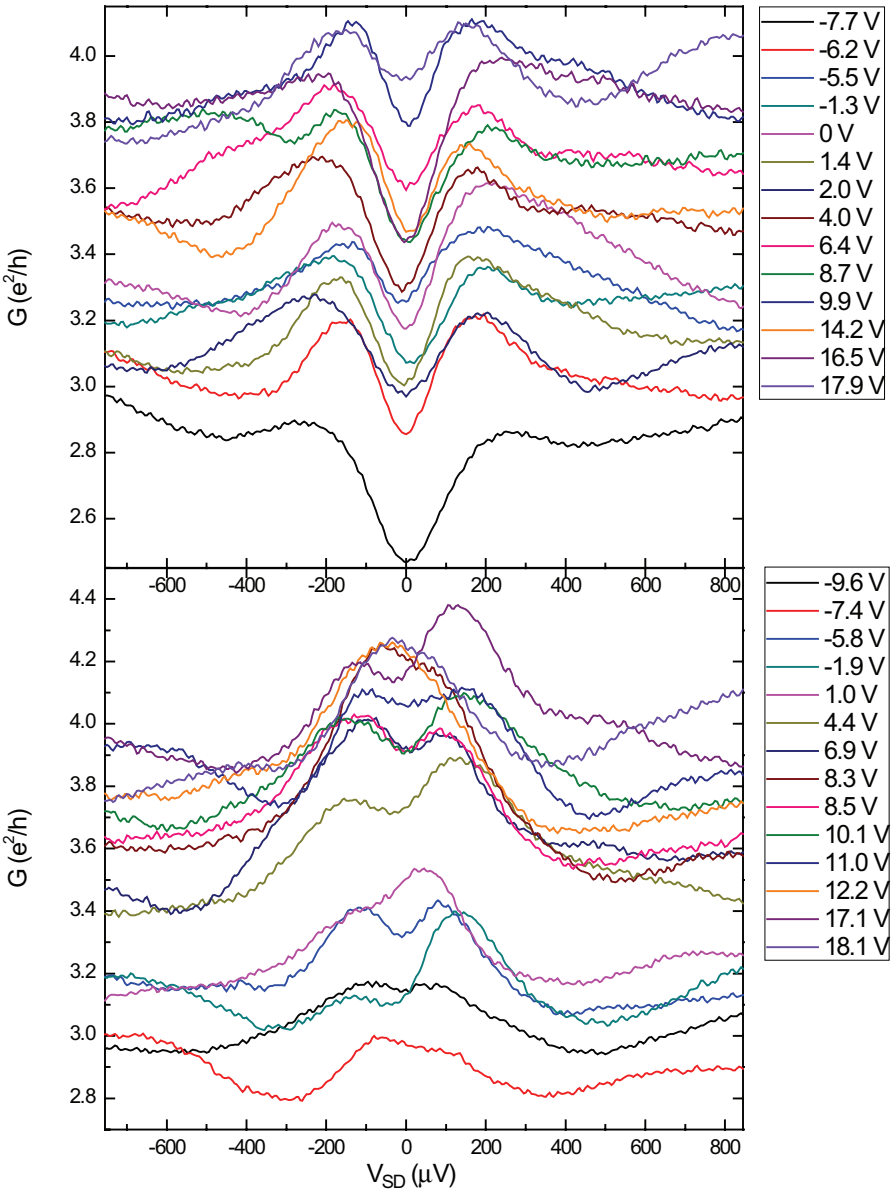

FIGURE 4.15.: Additional $G(V_{SD})$ traces for the S/Graphene/S structure with closely spaced ($d = 225$ nm) electrodes. Traces for gate voltages showing a superconducting gap are depicted in the upper graph, while those showing increased sub-gap conductance are plotted in the lower graph.

5. Conclusions and Outlook

During this master project, we simplified the fabrication of grids used for locating graphene flakes and established a convenient, semi-automatic method for making electron-beam lithography layout masks. We fabricated single-layer graphene (SLG) devices, as proven by the half-integer quantum Hall conductance plateaus.

In devices with four ferromagnetic PdNi/Co/Pd electrodes, we measured anisotropic magnetoresistance (AMR) signals of 0.25 %. In two-terminal and classical four-terminal magnetoresistance (MR) measurements, we observed magnetoresistive switching on the order of 1 - 2 %, and the switching fields could be attributed to the individual electrodes of different width. Non-local measurements of the same device were not conclusive, as two of the electrodes probably formed a point contact. In devices only containing Co and no PdNi, we observed only very weak AMR and MR signals.

In addition, we measured the conductance of a graphene nanoribbon contacted by superconducting Ti/Al/Ti electrodes. While the device showed no source-drain bias dependence with the electrodes in the normal state, we observed a conductance gap and Andreev reflection in the superconducting state. Upon applying an external (in-plane) magnetic field $B_{\parallel}$, these features were largely suppressed at $B_{\parallel} = 1\,\mathrm{T}$.

During this project, we have converged our goal of studying spin coherence effects in hybrid graphene devices. Since spin injection and Andreev reflection are sensitive to the interface transparencies, fabrication of clean as well as of well-defined tunnel barriers between graphene and the electrodes is an important aspect of this project. In the future, such tunnel barriers will be grown by atomic layer deposition (ALD). Much knowledge has also been gained in fabrication of cleaner graphene devices, which is essential for studying coherence effects.

Bibliography

[1] Kroto, H. W., Heath, J. R., O'Brien, S. C., Curl, R. F. & Smalley, R. E. C60: Buckminsterfullerene. *Nature* **318**, 162–163 (1985).

[2] Iijima, S. Helical microtubules of graphitic carbon. *Nature* **354**, 56–58 (1991).

[3] Novoselov, K. S. *et al.* Electric field effect in atomically thin carbon films. *Science* **306**, 666–669 (2004).

[4] Geim, A. K. & Novoselov, K. S. The rise of graphene. *Nat Mater* **6**, 183–191 (2007).

[5] Peierls, R. E. Quelques propriétés typiques des corps solides. *Ann. I. H. Poincaré* **5**, 177–222 (1935).

[6] Landau, L. D. Zur Theorie der Phasenumwandlungen II. *Phys. Z. Sowjetunion* **11**, 26–35 (1937).

[7] Meyer, J. C. *et al.* The structure of suspended graphene sheets. *Nature* **446**, 60–63 (2007).

[8] Ozyilmaz, B. *et al.* Electronic transport and quantum hall effect in bipolar graphene p-n-p junctions. *Physical Review Letters* **99**, 166804 (2007).

[9] Oostinga, J. B., Heersche, H. B., Liu, X., Morpurgo, A. F. & Vandersypen, L. M. K. Gate-induced insulating state in bilayer graphene devices. *Nat Mater* **7**, 151–157 (2007).

[10] Berger, C. *et al.* Ultrathin epitaxial graphite: 2D electron gas properties and a route toward graphene-based nanoelectronics. *Journal of Physical Chemistry B* **108**, 19912–19916 (2004).

[11] Tombros, N., Jozsa, C., Popinciuc, M., Jonkman, H. T. & van Wees, B. J. Electronic spin transport and spin precession in single graphene layers at room temperature. *Nature* **448**, 571–574 (2007).

[12] Aurich, H. *Fabrication and Electrical Characterization of Graphene.* Master's thesis, University of Basel (2007).

[13] Hill, E., Geim, A., Novoselov, K., Schedin, F. & Blake, P. Graphene spin valve devices. *IEEE Transactions on Magnetics* **42**, 2694–2696 (2006).

[14] Ferrari, A. C. *et al.* Raman spectrum of graphene and graphene layers. *Physical Review Letters* **97**, 187401 (2006).

[15] Novoselov, K. S. *et al.* Two-dimensional gas of massless dirac fermions in graphene. *Nature* **438**, 197–200 (2005).

[16] Zhang, Y., Tan, Y.-W., Stormer, H. L. & Kim, P. Experimental observation of the quantum hall effect and berry's phase in graphene. *Nature* **438**, 201–204 (2005).

[17] Katsnelson, M. I. Graphene: carbon in two dimensions. *Materials Today* **10**, 20–27 (2007).

[18] Wallace, P. R. The band theory of graphite. *Phys. Rev.* **71**, 622–634 (1947).

[19] Schönenberger, C. Bandstructure of graphene and carbon nanotubes: An exercise in condensed matter physics. University of Basel (2000).

[20] Datta, S. Graphene bandstructure (lecture). Purdue University (2004).

[21] Wilson, M. Electrons in atomically thin carbon sheets behave like massless particles. *Physics Today* **1**, 21–23 (2006).

[22] Hall, E. On a new action of the magnet on electric currents. *American Journal of Mathematics* **2** (1879).

[23] Klitzing, K. v., Dorda, G. & Pepper, M. New method for high-accuracy determination of the fine-structure constant based on quantized hall resistance. *Phys. Rev. Lett.* **45**, 494–497 (1980).

[24] Trauzettel, B. Von Graphit zu Graphen. *Physik Journal* **6**, 39–44 (2007).

[25] Heersche, H. B., Jarillo-Herrero, P., Oostinga, J. B., Vandersypen, L. M. K. & Morpurgo, A. F. Bipolar supercurrent in graphene. *Nature* **446**, 56–59 (2007).

[26] Williams, J. R., DiCarlo, L. & Marcus, C. M. Quantum hall effect in a gate-controlled p-n junction of graphene. *Science* **317**, 638–641 (2007).

[27] Williams, J. R., Abanin, D. A., DiCarlo, L., Levitov, L. S. & Marcus, C. M. Quantum Hall conductance of two-terminal graphene devices. *cond-mat:0810.3397* (2008).

[28] Abanin, D. A. & Levitov, L. S. Conformal invariance and shape-dependent conductance of graphene samples. *Phys. Rev. B* **78**, 035416 (2008).

[29] Lippmann, H. J. & Kuhrt, R. The geometrical influence of rectangular semiconductor plates on the hall effect. *Z. Naturforsch. A* **13**, 462 (1958).

[30] Dykhne, A. M. & Ruzin, I. M. Theory of the fractional quantum hall effect: The two-phase model. *Phys. Rev. B* **50**, 2369–2379 (1994).

[31] Wick, R. F. Solution of the field problem of the germanium gyrator. *Journal of Applied Physics* **25**, 741–756 (1954).

[32] Rendell, R. W. & Girvin, S. M. Hall voltage dependence on inversion-layer geometry in the quantum hall-effect regime. *Phys. Rev. B* **23**, 6610–6614 (1981).

[33] Jungwirth, T., Abolfath, M., Sinova, J., Kucera, J. & MacDonald, A. H. Boltzmann theory of engineered anisotropic magnetoresistance in (Ga,Mn)As. *Applied Physics Letters* **81**, 4029–4031 (2002).

[34] Julliere, M. Tunneling between ferromagnetic films. *Phys. Lett. A* **54**, 225–226 (1975).

[35] Baibich, M. N. *et al.* Giant magnetoresistance of (001)Fe/(001)Cr magnetic superlattices. *Phys. Rev. Lett.* **61**, 2472–2475 (1988).

[36] Binasch, G., Grünberg, P., Saurenbach, F. & Zinn, W. Enhanced magnetoresistance in layered magnetic structures with antiferromagnetic interlayer exchange. *Phys. Rev. B* **39**, 4828–4830 (1989).

[37] Zutic, I., Fabian, J. & Sarma, S. D. Spintronics: Fundamentals and applications. *Reviews of Modern Physics* **76**, 323 (2004).

[38] Jedema, F. J. *Electrical Spin Injection in metallic Mesoscopic Spin Valves.* Ph.D. thesis, University of Groeningen (2002).

[39] Pannetier, B. & Courtois, H. Andreev reflection and proximity effect. *TEMP.PHYS.* **118**, 599 (2000).

[40] Beenakker, C. W. J. Andreev reflection and Klein tunneling in graphene. *Colloquium* (2007).

[41] Minder, N. Towards non-local measurements of spin transport in graphene. Projektarbeit, University of Basel (2008).

[42] Blake, P. *et al.* Making graphene visible. *Applied Physics Letters* **91**, 063124 (2007).

[43] Lum, I., Mayer, M. & Zhou, Y. Footprint study of ultrasonic wedge-bonding with aluminum wire on copper substrate. *Journal of Electronic Materials* **35**, 433–442 (2006).

[44] Tinkham, M. *Introduction to Superconductivity.* McGraw-Hill (1996).

Appendix

A. Device Fabrication

Deposition of Ti/Au markers using UV lithography

Fabrication of markers using UV lithography is a lot faster than standard electron beam lithography (EBL). Naturally, the resolution of EBL by far exceeds that of UV lithography; in practice, the markers fabricated with UV lithography have nonetheless turned out to be a feasible alternative for locating and contacting graphene flakes. The production steps are as follows:

- Cut a Si wafer with 300 ± 5 nm SiO_2 into pieces of approximately 1×2 cm^2 using a diamond cutter.
- Spin *ma-N 415* negative photoresist (micro resist technology, Berlin, Germany) at a speed of 6000 rpm for 40 s and anneal it on a hot plate at 100° C for 90 s.
- Expose with UV light for 60 s using a UV lithography mask aligner together with the marker mask.
- Develop in *ma-D 332S*(micro resist technology GmbH) for 75 s, stop development under deionized H_2O, blow dry using nitrogen gas.
- Optionally, remove undeveloped photoresist with ozone or oxygen plasma etching.
- Using a thermal or electron gun evaporation system, evaporate approximately 10 nm of Ti as adhesion layer followed by 40 nm of Au at $p_{base} \leq 1 \cdot 10^{-6}$ mbar. Lift-off is done in acetone.

Fabrication of a graphene device

The basic steps for fabricating a graphene device consisting of a single or few layer graphene flake contacted by metallic electrodes are described below. The method can easily be expanded by introducing additional steps such as structuring of the graphene flakes by etching or multiple lithography/evaporation steps to fabricate more advanced devices.

- Clean a Ti/Au grid using reactive ion etching (RIE). P_{base}: $5{\cdot}10^{-5}$ mbar, $P_{process}$: 25 mTorr, flow: 16 sccm Ar/8 sccm O_2, power: 10 W, time: 10 min.
- After RIE immediately deposit mechanically exfoliated graphene in the SiO_2 surface: using a suitable tape, e.g. blue Nitto tape (Nitto Denko Corporation, Osaka, Japan), cleave highly oriented pyrolytic graphite (HOPG) multiple times by pressing the tape onto the HOPG and then cleaving the flakes by pressing two pieces of tape together. Try out this procedure on dummy samples first before pressing a piece of tape with freshly cleaved HOPG onto the cleaned grid using your thumb or a rubber eraser.
- Locate graphene flakes under an optical microscope and take pictures of the flakes with four surrounding markers using a digital camera. Under white-lite illumination, 300 nm SiO_2 substrates appear light purple while graphene flakes lead to a slight blue shift. Verify the thickness of the flakes using AFM (or raman spectroscopy) until you can estimate the number of layers from the contrast difference.
- Optionally, clean the sample by annealing in vacuum at 400° C for 1 hour.
- Spin PMMA 950 K (Allresist GmbH, Strausberg, Germany) diluted with isopropanol (IPA) at a speed of 4000 rpm for 40 s, bake in an oven at 175° C for 35 min.
- Using an image processor such as *GIMP* (`www.gimp.org`), increase the contrast of the picture and store it as a monochromatic bitmap. Then convert the file with the bitmap to cif converter of the *CleWin* package (WieWeb Software, Hengelo, Netherlands), scale the layout down such that the marker-to-marker distance matches the actual width of 200 μm and construct contacts around the graphene flake using *CleWin, ELPHY* (Raith GmbH, Dortmund, Germany) or any other mask layout application.
- Expose the layout with EBL using prior determined parameters. For an approximately 300 nm thick film of PMMA, the following parameters worked fine for a 250 μm writefield. Acceleration voltage: 20 kV, stage height: 11 mm, area dose: 250 $\mu As{\cdot}cm^{-2}$, area step size: 8 nm.
- Develop in a 3:1 mixture of IPA/MIBK (Methyl isobutyl ketone) for 60 to 90 s, clean in IPA for 5 min, blow dry under N_2 gas.
- Evaporate metal of choice, keeping in mind that a low chamber pressure reduces base metals from oxidizing. Lift-off in acetone.
- Glue sample to a sample holder, e.g. using silver paint or PMMA, and connect the sample with the sample holder using ultrasonic wire bonding. Measure the sample or store it in a vacuum chamber.

B. Superconducting transition temperature of Ti/Al contacts

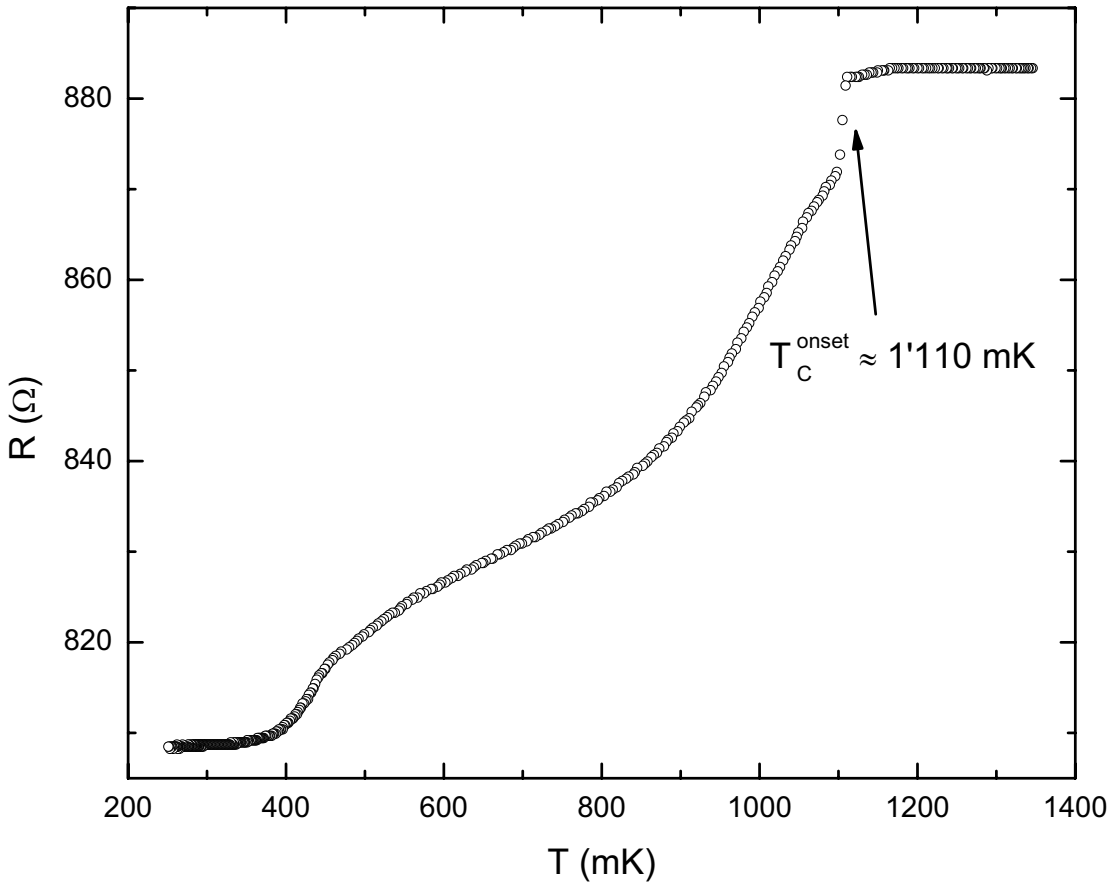

FIGURE 5.1.: Current-biased two-terminal $R(T)$ measurement of two superconducting Ti/Al (4.5/53.0 nm) electrodes on a multi-layer graphene flake (sample NM013) showing a superconducting transition temperature T_c^{onset} of 1'110 mK.

C. Source-drain bias dependence of SLG in perpendicular magnetic fields

The source-drain bias dependence on the conductance, $G(V_{SD})$, was studied on the single layer graphene (SLG) flake (sample NM063). Figure 5.2 shows grayscale plots of the two-terminal conductance $G(V_{SD}, V_{BG})$ at perpendicular magnetic fields $B_\perp = 6$T and 8T. In the region of the two central ($N = 0$) quantum Hall conductance plateaus, we observed an asymmetric bias dependence of the conductance.

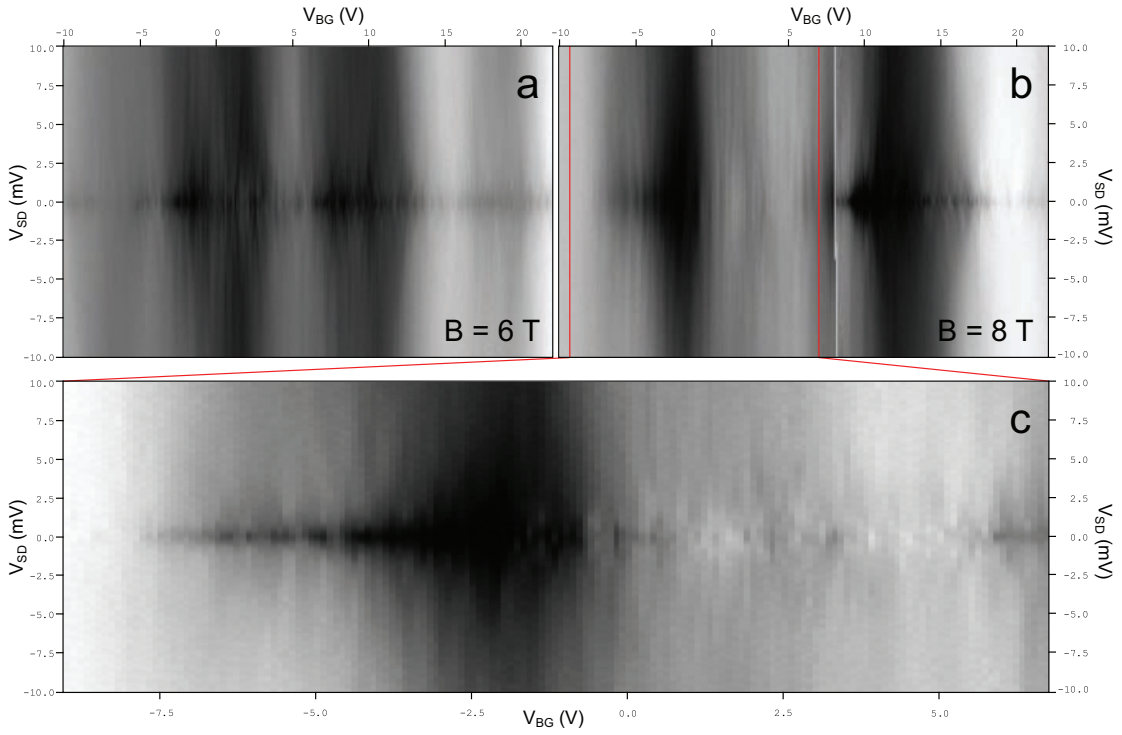

FIGURE 5.2.: **Source drain bias dependence of SLG**. Figures **a** and **b** show $G(V_{SD}, V_{BG})$ grayscale plots of the two-terminal conductance measurements of a single layer graphene sheet at $B_\perp = 6$T and 8T. Black and white areas denote low and high conductance. The enlarged region in **c** shows a diamond-like region of low conductance. The measurements were performed at $T = 240$ mK.